

# HST/ACS H $\alpha$ Imaging of the Carina Nebula: Outflow Activity Traced by Irradiated Herbig-Haro Jets<sup>\*</sup>

Nathan Smith<sup>1†</sup>, John Bally<sup>2</sup>, & Nolan R. Walborn<sup>3</sup>

<sup>1</sup>*Department of Astronomy, University of California, 601 Campbell Hall, Berkeley, CA 94720, USA*

<sup>2</sup>*Center for Astrophysics and Space Astronomy, University of Colorado, 389 UCB, Boulder, CO 80309, USA*

<sup>3</sup>*Space Telescope Science Institute, 3700 San Martin Dr., Baltimore, MD 21218, USA*

Accepted 0000, Received 0000, in original form 0000

## ABSTRACT

We report the discovery of new Herbig-Haro (HH) jets in the Carina Nebula, and we discuss the protostellar outflow activity of a young OB association. These are the first results of an H $\alpha$  imaging survey of Carina conducted with the *Hubble Space Telescope*/Advanced Camera for Surveys. Adding to the one previously known example (HH 666), we detect 21 new HH jets, plus 17 new candidate jets, ranging in length from 0.005 to 3 pc. Using the H $\alpha$  emission measure to estimate jet densities, we derive jet mass-loss rates ranging from  $8 \times 10^{-9}$  to  $\sim 10^{-6} M_{\odot} \text{ yr}^{-1}$ , but a comparison to the distribution of jet mass-loss rates in Orion suggests that we may be missing a large fraction of the jets below  $10^{-8} M_{\odot} \text{ yr}^{-1}$ . A key qualitative result is that even some of the smallest dark globules with sizes of  $\lesssim 1''$  (0.01 pc) are active sites of ongoing star formation because we see HH jets emerging from them, and that these offer potential analogs to the cradle of our Solar System because of their proximity to dozens of imminent supernovae that will enrich them with radioactive nuclides like  $^{60}\text{Fe}$ . Whereas most protoplanetary candidates identified from ground-based data are dark cometary globules, *HST* images now reveal protoplanetary structures in the core of the Tr 14 cluster, only 0.1–0.2 pc from several extreme O-type stars. Throughout Carina, some HH jets have axes bent away from nearby massive stars, while others show no bend, and still others are bent *toward* the massive stars. These jet morphologies serve as “wind socks”; strong photoevaporative flows can shape the jets, competing with the direct winds and radiation from massive stars. We find no clear tendency for jets to be aligned perpendicular to the axes of dust pillars. Finally, even allowing for a large number of jets that may escape detection, we find that HH jets are negligible to the global turbulence of the surrounding region, which is driven by massive star feedback.

**Key words:** ISM: Herbig-Haro objects – ISM: individual (NGC 3372, NGC 3324) – ISM: jets and outflows – stars: formation – stars: pre-main-sequence

## 1 INTRODUCTION

The Carina Nebula (NGC 3372) provides us with a rich and unique laboratory in which to perform detailed study of massive-star feedback on a surrounding second generation of newly formed stars. It offers our best available trade-off between an extreme population of the most massive O-type stars known, weighed against its nearby distance and

relatively low interstellar extinction. The central star clusters Tr 14 and Tr 16 (e.g., Massey & Johnson 1993) are famous for their collection of extremely massive stars, including  $\eta$  Car (Davidson & Humphreys 1997), three WNH stars (see Smith & Conti 2008, and references therein), several of the earliest O-type stars known including the O2 supergiant HD 93129A (Walborn et al. 2002), and dozens of additional O-type stars. See Walborn (2009) and Smith (2006a) for recent reviews of Carina’s remarkable massive-star content and its collective energy input, and see Smith & Brooks (2007) for a recent census of the global nebulaosity and integrated mass/energy budgets of the region.

Surrounding the bright central clusters, one finds evidence for active ongoing star formation, particularly in the

<sup>\*</sup> Based on observations made with the NASA/ESA *Hubble Space Telescope*, obtained at the Space Telescope Science Institute, which is operated by the Association of Universities for Research in Astronomy, Inc., under NASA contract NAS5-26555.

<sup>†</sup> Email: nathans@astro.berkeley.edu

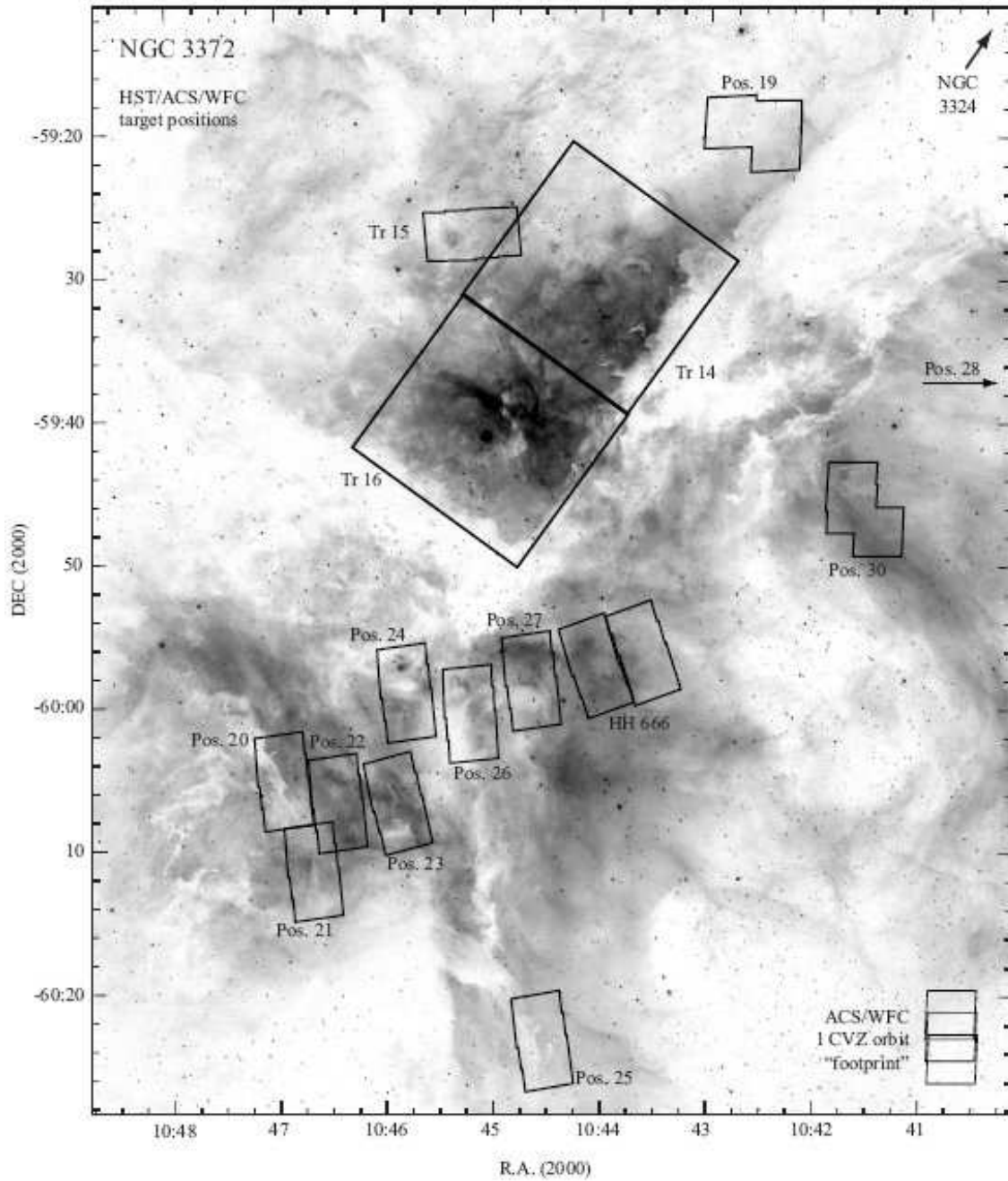


**Figure 1.** A large-scale  $H\alpha$  image of the Carina Nebula obtained with the Curtis-Schmidt telescope at CTIO (from Smith 2002). Positions of *HST* observations are indicated. Most target positions used a “footprint” composed of three individual dithered exposures in a single CVZ orbit, shown at the lower right corner. In a few cases, this pattern was modified to suit the particular target (Positions 19 and 30). In the central region, two large mosaics of the regions around Tr14 and Tr16 were composed of eight of these footprints each to yield a large contiguous mosaic of the inner nebula. Two pointings are not shown here: one in the neighboring H II region NGC 3324, and one in the far-western part of Carina (Pos. 28).

collection of dust pillars to the south (Smith et al. 2000; Smith & Brooks 2007; Megeath et al. 1996; Rathborne et al. 2004). Smith & Brooks (2007) pointed out, however, that the current star formation activity appears less vigorous than the first generation of star formation that yielded Tr 14 and Tr 16. They conjectured that this is because most of the present-day nebular mass budget consists of warm atomic gas in photodissociation regions (PDRs) and not in cold

molecular cloud cores, so that most of the gas mass reservoir is not currently able to participate in new star formation. Star formation appears to be “percolating” in many smaller clouds in Carina, inhibited by the strong UV radiation from O stars in the region. These  $\sim 70$  O stars are destined to explode as supernovae (SNe) soon, which will rob the region of its UV radiation and will sweep these clouds into dense

**Table 1.** ACS Observation Log

Target	$\alpha_{2000}$	$\delta_{2000}$	Date	P.A.( $^{\circ}$ )	Orbits	Comment
N3324	10:36:55	-58:38:05	2006 Mar 7	9.7	1	edge-on I.F.
Tr 14	10:44:00	-59:30:50	2005 Jul 17	144.0	8	edge-on I.F., dust pillars, globules
Tr 15	10:45:10	-59:27:00	2006 Nov 26	95.0	1	globules near Tr15
Tr 16	10:44:55	-59:41:10	2005 Jul 18	144.0	8	Keyhole, $\eta$ Car, globules, etc.
HH 666	10:43:50	-59:56:40	2005 Mar 30	20.0	2	south pillars, Axis of Evil
Pos 19	10:42:30	-59:19:50	2006 Mar 8	8.9	1	globules
Pos 20	10:47:00	-60:05:00	2006 Mar 2	8.0	1	dark globules, Bo 11
Pos 21	10:46:40	-60:12:00	2006 Mar 4	8.0	1	south pillars
Pos 22	10:46:25	-60:06:40	2006 Mar 4	8.0	1	globules
Pos 23	10:45:53	-60:06:40	2005 Mar 28	15.0	1	south pillars
Pos 24	10:45:49	-59:59:00	2006 Mar 2	8.0	1	south pillars, Treasure Chest cluster
Pos 25	10:44:31	-60:23:10	2005 Sep 10	10.0	1	globules
Pos 26	10:45:13	-60:00:20	2006 Mar 2	5.8	1	south pillars
Pos 27	10:44:40	-59:58:00	2006 Mar 7	8.3	1	south pillars
Pos 28	10:38:52	-59:35:50	2006 Apr 20	75.0	1	dust pillars, west
Pos 30	10:41:33	-59:44:00	2005 Sep 11	10.7	1	dust pillars, west edge

clumps. In this way, Smith & Brooks (2007) speculated that a new wave of star formation may occur in the near future.

The imminent explosion of several dozen SNe has implications for the new generation of stars currently forming in cometary clouds and dust pillars only 5–30 pc away. Namely, the clouds from which these young stars form will soon be pelted by ejecta from numerous SNe over a relatively short time period. SN ejecta contain radioactive nuclides such as  $^{60}\text{Fe}$ ,  $^{26}\text{Al}$ , and other materials found in Solar-System meteorites, which require that a nearby SN injected processed material into the presolar cloud or disk (Lee et al. 1976; Cameron & Truran 1977; Tachibana & Huss 2003; Hester et al. 2004; Desch & Ouellette 2005; Boss et al. 2008; Vanhala & Boss 2000, 2002). Thus, Smith & Brooks (2007) argued that regions like the South Pillars may provide a close analog to the cradle of our own Solar System.

Whether or not SN explosions have already occurred in Carina is still a topic of current research. SNe are not required for the global energy budget (Smith & Brooks 2007), but high velocity gas seen in absorption (Walborn et al. 2007; and references therein) and the recent discovery of a neutron star in the field (Hamaguchi et al. 2009) imply that a recent SN occurred here. However, this SN may be projected along our line-of-sight to Carina rather than *inside* it (Walborn et al. 2007). In any case, Carina provides a laboratory in which to study a new generation of young stars exposed to feedback from an extreme population of massive stars. Here, we focus on the outflows that are a signpost of embedded protostars caught in an active accretion phase.

Herbig-Haro (HH) objects are nebulosities associated with protostellar outflows that are identified at visual wavelengths, usually by their shock-excited emission in lines like H $\alpha$  and [S II] (see Reipurth & Bally 2001 for a review). Since they arise in protostellar outflows, HH jets are signposts of actively accreting young stars embedded within dark clouds. When their physical properties can be measured accurately, they can be used to estimate the jet mass, momentum, kinetic energy, and mass-loss rate, and hence, the injection of energy and turbulence into the surrounding interstellar medium (ISM). They also provide a way to constrain the recent jet mass-loss history and to infer the past accretion rate of the underlying star. Large-format array detectors applied to nearby outflows have revealed HH objects from single flows more than a parsec in length (e.g., Reipurth et

al. 1997b; Devine et al. 1997; Eisloffel & Mundt 1997), providing a record of the accretion history of the driving star over the previous  $\sim 10^4$  yr — a significant fraction of the most active accretion phase.

In most cases of nearby jets in low-mass star-forming regions, the nebular emission arises from collisional excitation in shocks, so observations can only trace the jet material that was very recently heated by passage through a shock. Much of the remaining jet material may therefore be invisible, making estimates of the physical parameters difficult. In the presence of a strong external UV radiation field provided by nearby OB stars, however, even unshocked jet material is rendered visible when it is photoionized. Such irradiated HH jets (Reipurth et al. 1998; Bally & Reipurth 2001) emit visual-wavelength spectra characteristic of photoionized gas, making it easier to constrain the physical properties of the jet using standard photoionization theory. Even in the absence of spectra, the H $\alpha$  surface brightness in images can be used to infer the emission measure  $EM \propto \int n_e^2 dl$ , and hence, the electron density of the jet  $n_e$ , providing that the emitting path length  $dl$  can be estimated from the spatially resolved jet geometry in high-resolution images such as those attainable with the *Hubble Space Telescope* (HST).

With its active ongoing star formation and strong UV radiation field, Carina provides fertile hunting ground in which to identify a large population of irradiated HH jets. So far, the only HH jet to have been discovered in Carina is HH 666 (Smith et al. 2004c), which is a parsec-scale bipolar jet emerging from one of the South Pillars. The embedded infrared (IR) source that drives the outflow was also identified (Smith et al. 2004c). Its discovery in ground-based images was enabled by the fact that it is such a large and particularly bright jet. One might expect that many other HH jets are lurking in such a rich region, but that they are difficult to see at ground-based angular resolution because their thin filaments and shocks are drowned in the bright background nebular light.

In this paper we show that HH 666 was the tip of the iceberg, with many more HH jets and candidates seen in our HST images. Throughout, we adopt the precise distance to Carina of  $2300(\pm 50)$  pc derived from the expansion kinematics of the Homunculus Nebula around  $\eta$  Carinae by Smith (2006b), which is known to reside within the center of the Carina Nebula rather than being projected along the same

**Table 2.** HH Jets in Carina and NGC 3324

HH	$\alpha_{2000}$	$\delta_{2000}$	P.A.( $^{\circ}$ )	Pointing	Comment
666	10:43:51.3	-59:55:21	293.5	HH 666	Previously discovered
900	10:45:19.3	-59:44:23	242	Tr 16	small glob., points to $\eta$ Car
901	10:44:03.5	-59:31:02	279	Tr 14	pillar head, points to Tr14
902	10:44:01.7	-59:30:32	258	Tr 14	pillar head, points to Tr14
903	10:45:56.6	-60:06:08	278	Pos 23	side of large pillar
1002	10:36:57.1	-58:37:26	106	NGC 3324	edge-on I.F.
1003A	10:36:53.6	-58:38:09	171	NGC 3324	jet body, near I.F.
1003C	10:36:54.8	-58:39:09	171	NGC 3324	bow shock
1004	10:46:44.8	-60:10:20	247	Pos 21	pillar head, bipolar
1005	10:46:44.2	-60:10:35	112	Pos 21	same pillar as HH 1004
1006	10:46:33.0	-60:03:54	352	Pos 22	propylid cand., bipolar
1007	10:44:29.5	-60:23:05	270	Pos 25	irregular
1008	10:44:47.0	-59:57:25	170	Pos 27	large bow shock, from pillar head?
1009	10:44:39.5	-59:58:26	?	Pos 27	irregular
1010	10:41:48.7	-59:43:38	215	Pos 30	dark pillar head, bipolar
1011	10:45:04.9	-59:26:59	260	Tr 15	small glob., one-sided jet
1012	10:44:38.6	-59:30:07	140	Tr 14	LL Ori object, microjet
1013	10:44:19.2	-59:26:14	35	Tr 14	propylid, bow shock, microjet
1014	10:45:45.9	-59:41:06	290	Tr 16	pillar head, toward $\eta$ Car
1015	10:44:27.9	-60:22:57	315	Pos 25	pillar head
1016	10:45:53.2	-59:56:05	320	Pos 24	pillar head, Treasure Chest
1017	10:44:41.5	-59:33:57	25	Tr14	jet bends away from Tr 14
1018	10:44:52.9	-59:45:26	332	Tr16	microjet and shock

**Table 3.** Candidate Jets in Carina and NGC 3324

HH	$\alpha_{2000}$	$\delta_{2000}$	P.A.( $^{\circ}$ )	Pointing	Comment
c-1 (3324)	10:36:55.9	-58:36:38	90	NGC 3324	edge-on I.F.
c-2 (3324)	10:37:01.1	-58:38:37	?	NGC 3324	shocks, unclear source
c-1	10:44:05.4	-59:29:40	300	Tr 14	propylid cand.
c-2	10:36:55.9	-58:36:38	5	Pos 27	pillar head, unclear morph.
c-3	10:45:04.6	-60:03:02	?	Pos 26	small glob., unclear morph.
c-4	10:45:08.3	-60:02:31	?	Pos 26	bow shock?
c-5	10:45:09.3	-60:01:59	298	Pos 26	pillar head, coll. chain of knots
c-6	10:45:09.3	-60:02:26	2	Pos 26	pillar side, bipolar, par. to I.F.
c-7	10:45:13.4	-60:02:55	165?	Pos 26	bow shock? unclear source
c-8	10:45:12.2	-60:03:09	?	Pos 26	LL Ori object?
c-9	10:45:08.0	-59:31:03	275?	Tr 14	large bow shock, unclear source
c-10	10:45:57.2	-60:05:32	230	Pos 23	pillar head, bow shocks?
c-11	10:46:36.0	-60:07:12	225	Pos 22	bow shock, unclear source
c-12	10:45:07.8	-60:03:23	?	Pos 26	shock, unclear source
c-13	10:44:00.6	-59:54:27	169	HH 666	microjet from star near HH 666
c-14	10:45:43.7	-59:41:39	?	Tr 16	curved shocks near HH 1014
c-15	10:43:54.6	-59:32:46	80	Tr 14	core of Tr 14, microjet

sightline (Allen 1979; Lopez & Meaburn 1986; Walborn & Liller 1977). We describe the *HST* observations in §2. In §3 we provide an overview of the new HH jets and HH jet candidates; §3 is detailed and largely descriptive, so readers may wish to only skim this section and refer back to it when interested in a specific object. §4 takes a closer look at three remarkable bipolar jets, while §5 investigates the distribution of mass-loss rates. We discuss main points in §6, and we provide a short conclusion in §7.

## 2 OBSERVATIONS: THE ACS H $\alpha$ SURVEY OF THE CARINA NEBULA

We present images covering a large portion of the Carina Nebula, comparable to our previous H $\alpha$  mapping of the Orion Nebula with *HST* (Bally et al. 2005, 2006; Smith et al. 2005b). With a similar setup, we used the Wide-Field Channel (WFC) of *HST*'s Advanced Camera for Surveys (ACS) under joint programs GO-10241 and GO-10475 (PI: Smith) conducted in Cycles 13 and 14.

Because of the large area of the Carina Nebula (several

square degrees), it was impractical to make a single contiguous map of the entire region with *HST* as we had done in Orion. Instead, we conducted the survey in two phases. First, during Cycle 13 we made a large (13'6 $\times$ 27') contiguous mosaic image of the brightest inner parts of Carina surrounding the clusters Tr14 and Tr16, including the Keyhole Nebula and  $\eta$  Carinae. Second, we selected several individual pointings at various positions in the nebula. These targets were chosen because they were deemed to have more potential to yield interesting results related to ongoing star formation (protoplanetary disks, globules, outflows, embedded sources, young star clusters) based on their structure in our previous ground-based narrow-band survey of the entire Carina region with the Cerro Tololo Inter-American Observatory (CTIO) 4m telescope (e.g., Smith et al. 2003).

The ACS/WFC aperture positions we targeted are shown in Figure 1, and the individual target positions and observation dates are listed in Table 1. The target positions in Table 1 are the approximate centers of each group of off-set pointings defining one "visit". We were able to maximize the efficiency of these observations (area covered per orbit)

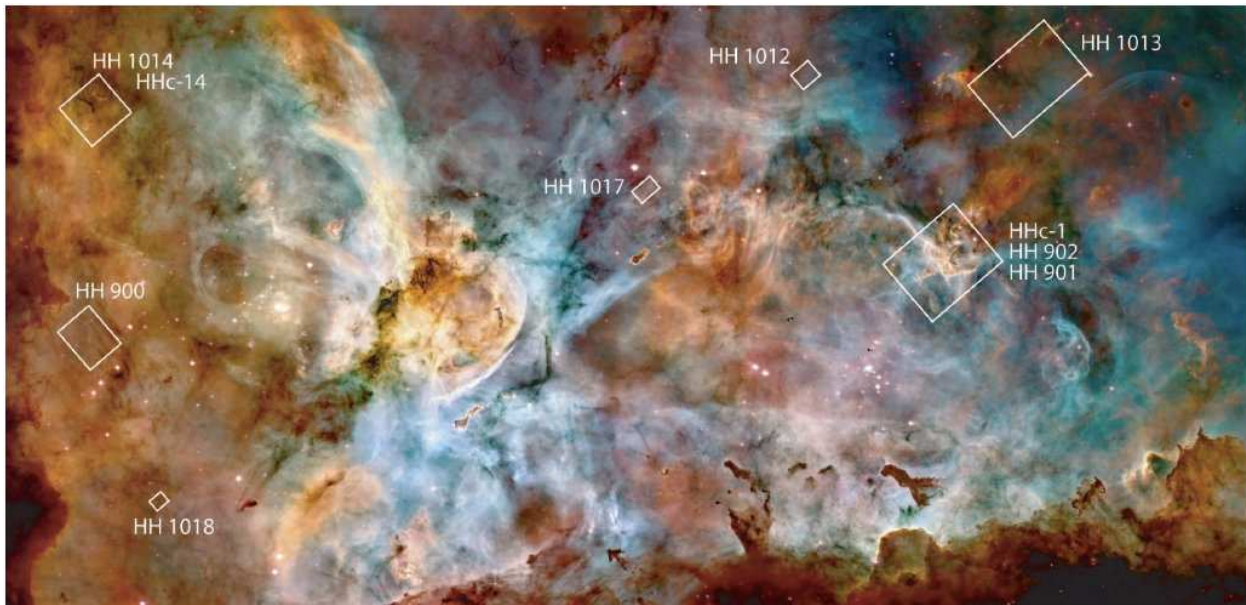


**Figure 2.** The color Hubble Heritage image of the inner Carina Nebula including the Tr 14 and Tr 16 clusters, the Keyhole, and  $\eta$  Carinae, plus several newly discovered HH jets. This is made from a large ACS H $\alpha$  mosaic used for the intensity scale in the image, while the color coding is taken from ground-based narrow-band images obtained with the MOSIAC camera on the 4m Blanco telescope at CTIO (from Smith et al. 2003), with [O III] in blue, H $\alpha$  in green, and [S II] in red. This ground-based image was also used to patch small gaps in the ACS mosaic. See the Hubble Heritage webpage for more information about the image processing for this large mosaic, where color images for individual jets and other structures can be found as well (<http://heritage.stsci.edu>). The full field shown here is roughly  $12' \times 25'$ . The rectangular boxes show the detailed fields of view for various HH jets included in the large mosaic. North is to the upper right; the small boxes around individual HH jets are aligned with R.A. and DEC directions.

because Carina is far enough south that all orbits were conducted in continuous viewing zone (CVZ) mode. Given the restrictions of the ACS buffer, this allowed for a maximum of 6 individual exposures per orbit. The observations during each orbit were identical, consisting of 3 pairs of CR-SPLIT exposures to correct for cosmic rays and hot pixels. We used the F658N filter (transmitting both H $\alpha$  and [N II]  $\lambda 6583$ ), with a total exposure time of 1000 s at each position (500 s per individual exposure). For each CVZ orbit, we adopted a 3-position linear offset pattern that maximized the area covered on the sky while also filling-in the inter-chip gap on the ACS detector. This typical ACS 1-orbit “footprint” is shown in the lower right corner of Figure 1, covering a rectangular  $205'' \times 400''$  region. The large square regions representing the contiguous maps of the Tr14 and Tr16 regions (Figure 2) each consisted of 8 of these footprints. In two cases, positions 19 and 30, this offset pattern was modified slightly to include interesting targets while compensating for roll-angle and scheduling restrictions; see Fig. 1. Two positions, the adjacent region NGC 3324 and Position 28, are not shown in Figure 1 because they are too far outside the field of view.

The total area on the sky covered by our ACS imaging was roughly 706 arcmin<sup>2</sup>. This program includes the first *HST* imaging of the Carina Nebula for  $\sim 98\%$  of the area we surveyed. Prior to this program, only small regions around  $\eta$  Car (e.g., Morse et al. 1998; Smith et al. 2005a; Currie et al. 1996) and the Keyhole<sup>1</sup> had been imaged with the Wide Field Planetary Camera 2 (WFPC2), and very small

regions in the core of the Tr14 cluster and  $\eta$  Car itself were imaged with ACS’s High Resolution Channel (ACS/HRC) (e.g., Smith et al. 2004b; Maíz Apellániz et al. 2005). The ACS/WFC images were reduced and combined using the PYRAF routine MULTIDRIZZLE, with manually determined pixel shifts using the pipeline-calibrated, flat-fielded individual exposures. MULTIDRIZZLE combines exposures, generates static bad-pixel masks, corrects for image distortions, and removes cosmic rays using the CR-SPLIT pairs. In this paper we report the discovery of several new HH jets in Carina. Other new results from this *HST* imaging program will be presented in future papers.

### 3 RESULTS

#### 3.1 New HH Jets and Candidate Jets

We carefully searched the full area covered by all frames in our ACS/WFC survey of the Carina Nebula and NGC 3324 in order to identify protostellar outflows visible in H $\alpha$  emission. This identification process is necessarily subjective without multi-epoch *HST* images to detect proper motions (e.g., Bally et al. 2006; Smith et al. 2005b) and without high-resolution spectra of all sources to separate Doppler-shifted jet emission from the background. (These techniques will be used in the future to confirm or reject candidate sources and to identify new flows.) HH jets were identified by nebular

<sup>1</sup> The Hubble Heritage Image of the Keyhole Nebula is available

from <http://opposite.stsci.edu/pubinfo/pr/2000/06/>; see also Smith et al. 2004a.

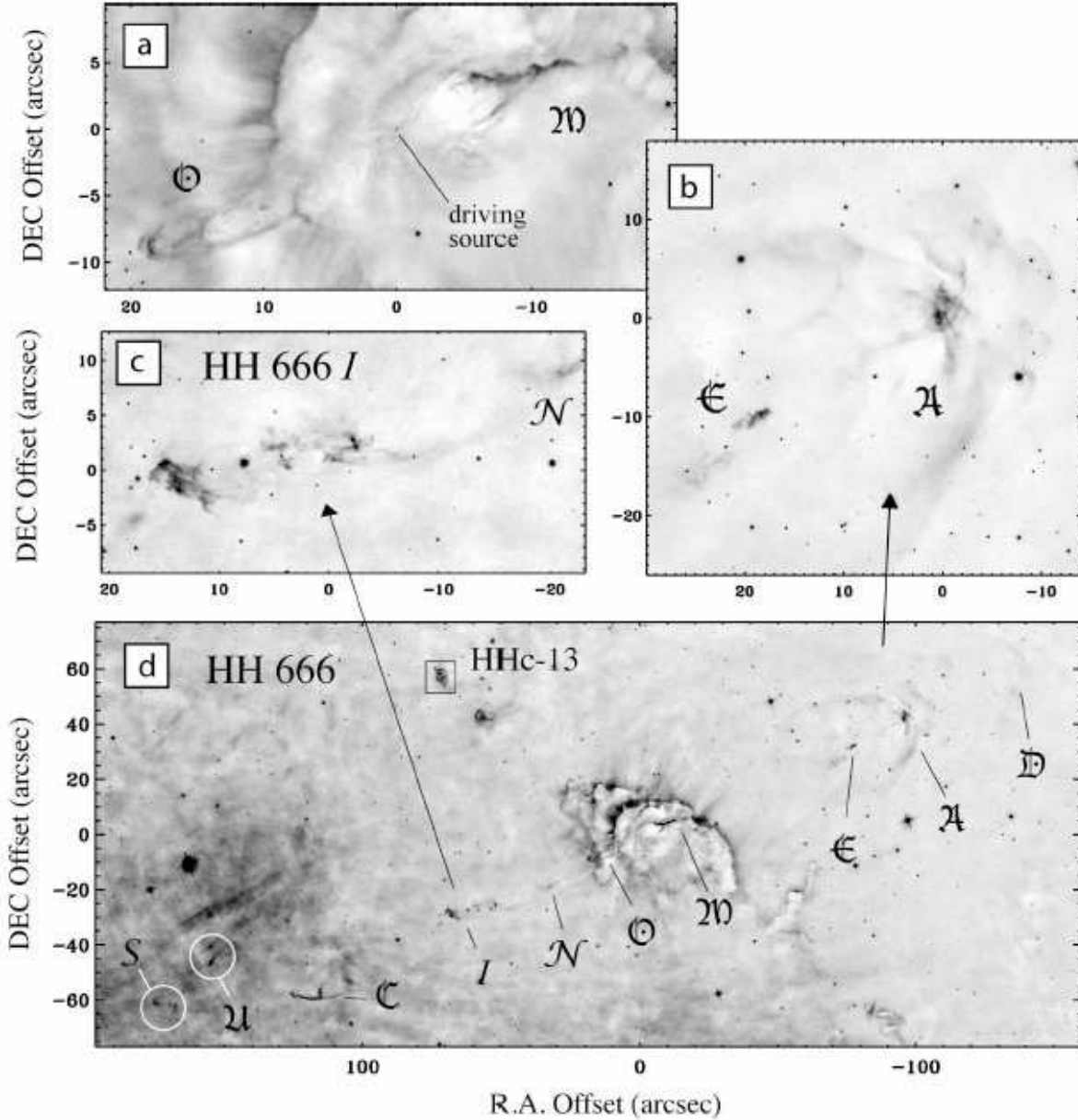


**Figure 3.**  $H\alpha$  images of the field including the Axis of Evil, HH 666. Panels (a, b, c) show details of features within the flow, whereas Panel (d) shows the full bipolar jet. Panel (a) is the center of the flow including the putative driving source, HH 666 IRS1, and the collimated inner jet features HH 666 M and O. Panel (b) shows the main bow shock HH 666 A and an internal shock in the flow, HH 666 E. Panel (c) shows shock structures within the flow, HH 666 N and I. The full bipolar jet in Panel (d) includes two new shocks seen in the ACS images, HH 666 U and S (lower left), which were not seen in ground-based images (Smith et al. 2004c). The location of HHc-13 is also identified (see §3.4.9).

features showing well-structured parabolic bow-shocks and Mach disks, resembling the morphology seen in objects such as HH 34, HH 47, and HH 111 (Reipurth et al. 1997b, 2002; Heathcote et al. 1996; Hartigan et al. 1999, 2001; Morse et al. 1992, 1994), or by high-contrast emission from the body of a collimated flow, and in some cases the likely counter flow. A list of new HH jet sources is given in Table 2, and a list of HH jet candidates for which the jet nature is less clear is given in Table 3. HH 666 has been previously discovered in ground-based data (Smith et al. 2004c), but is included in Table 2 for completeness. The discovery of all other HH

jets and candidate sources is reported here for the first time. Individual sources are discussed below.

### 3.2 Comments on individual Jets

#### 3.2.1 HH 666

HH 666, the so-called “Axis of Evil”, is the only jet in Carina that could be confidently identified in ground-based data. Smith et al. (2004c) discovered this remarkable jet and presented a detailed analysis of ground-based images and spec-



tra. It is a linear bipolar jet emerging from the head of a dark dust pillar that points toward  $\eta$  Carinae. It has a projected length of  $4\frac{1}{5}$  on the sky, and with a total length of over 3 pc, HH 666 is one of the longest HH jets known (see Devine et al. 1997; Eislöffel & Mundt 1997). Optical images show a chain of dense knots along the jet axis and a clear bow shock/Mach disk pair (HH 666 A) at the main terminal working surface. Along the jet axis, near-IR images reveal an embedded Class I protostar inside the globule that is the presumed driving source of the flow, with  $L \simeq 210L_{\odot}$ . Narrow-band near-IR images show bright [Fe II]  $\lambda 16435$  emission from the obscured parts of the jet inside the globule, connecting the parsec-scale outflow seen at visual wavelengths to the embedded inner IR point source. Long-slit echelle spectra revealed a coherent outflow pattern, with the south-east part of the flow being redshifted and the north-west flow being blueshifted. These spectra revealed Doppler shifts of more than  $\pm 200 \text{ km s}^{-1}$ , and a velocity pattern consistent with a sequence of individual Hubble-like flows along the jet axis. This provided suggestive evidence that the jet was formed by a series of discrete, episodic mass-loss events rather than a continuous steady outflow, perhaps related to the class of FU Ori outbursts (Hartmann & Kenyon 1985).

Our new ACS/WFC image of HH 666 is shown in Figure 3. The entire flow is shown in Figure 3d, while Figures 3a, 3b, and 3c zoom-in on the base of the jet where it breaks out of the globule, the main working surface HH 666 A, and an internal working surface HH 666 I, respectively. The morphology seen in the new *HST*  $H\alpha$  image confirms that the features HH 666 D, A, E, M, O, N, I, and C are shock structures in the HH 666 flow along the jet axis, and not small irradiated clouds. The *HST* image also reveals two new shock structures that we denote HH 666 U and HH 666 S at the eastern end of the flow. Together, HH 666 C, U, and S may compose a larger fragmented curved bow shock that is the eastern flow's analog of HH 666 A. A terminus of the eastern flow was not apparent in our ground-based study, but fainter structures are hard to detect here because the background nebula is brighter than near HH 666 A.

Some of the most intriguing new results from the *HST* images of HH 666 concern the inner structure of the jet near the driving source, detailed in Figure 3a. A faint star is detected along the jet axis at roughly the same position as the IR source that we proposed to be the driving source of the HH 666 jet (Smith et al. 2004c). This faint star exhibits low-level extended emission to the west along the jet axis, so we consider it likely that this is indeed the driving source of the outflow seen in the  $H\alpha$  filter despite the considerable extinction to the central star. HH 666 M and 666 O are the blueshifted and redshifted components, respectively, of the inner collimated jet that is also seen to be very bright in [Fe II]  $\lambda 16435$  traced back to the IR driving source (Smith et al. 2004c).

The detailed structure of HH 666 M is intriguing (Figure 3a). At about  $12''$ – $15''$  northwest of the star, the jet body is well-collimated along the jet axis. As we head eastward, back toward the driving source along the jet, the brightest emission bends to the north off the jet axis before it can reach all the way back to the driving source, seeming to curve around a prominent dark patch located immediately north-west of the driving source. This is true for the brightest line emission in the IR as well (Smith et al.

2004c), so it is not merely an obscuration effect as the jet passes behind the dark globule, for example. The surprising structure revealed by *HST* shows additional filamentary emission structures at other positions around the dark globule that *also* seem to merge with the collimated jet axis by the time they reach  $\sim 10''$  north-west of the driving source. It is almost as if the jet body has been divided into several streams as it is diverted around the surface of a dark object in its path. On the other hand, the dark oval along the flow axis may not be an obscuring globule, but rather, a cavity that is dark because a hole is punched into a dark cloud.

In any case, the jet flow then converges again beyond this dark feature to form a narrow jet. While there are many known cases of variability in collimation, mass-loss rate, speed, and orientation along a given flow (e.g., Reipurth & Bally 2001), HH 666 M is one of the clearest and most dramatic examples of recollimation in a protostellar jet. Mundt et al. (1991) discussed other possible examples such as HH 24G. The specific cause of the recollimation is not clear; it may indicate variable collimation with time, the apparently poor collimation may be caused by transverse motions as fast material overtakes slower material in the jet, or it may be a hydrodynamic refocussing of the jet as in a “Cantó nozzle” (Cantó et al. 1981) in objects like HH 526 in Orion (Bally et al. 2000).

The main terminal bow shock of the blueshifted north-western flow, HH 666 A, is shown in Figure 3b. This field also includes the internal working surface HH 666 E along the jet axis. HH 666 A is a huge bow shock extending over  $\sim 40''$  and spreading  $\sim 15''$  on either side of the jet axis. While HH 666 A maintains its overall parabolic shape seen earlier, at *HST* resolution it exhibits a more fragmented structure implying a series of overlapping shock arcs running into a mildly inhomogeneous medium. This irregular shock front is reminiscent of the complicated structure seen in HH 1 & 2 (Bally et al. 2002) or HH 168 (Hartigan et al. 2000). The peak emission is still dominated by what appears to be a Mach disk or reverse shock along the jet axis, which shows complex small scale structure including multiple dense knots and filaments, and resembles reverse shocks in well-studied nearby HH jets such as HH 47 (Heathcote et al. 1996; Morse et al. 1994) and HH 34 (Reipurth et al. 2002; Morse et al. 1992). Part of the forward shock along the jet axis extends ahead of the putative Mach disk by  $\sim 10''$  (0.1 pc). Multi-filter imaging or spatially resolved spectroscopy with *HST* could resolve the post-shock cooling zone.

The complex structure of an internal working surface in the flow is exemplified by HH 666 I, shown in Figure 3c. It is perhaps not surprising that compared to ground-based images (Smith et al. 2004c), the  $H\alpha$  emission structure seen with *HST* breaks up into a series of smaller clumps, filaments, and numerous thin arcs. These multiple shock structures indicate that even at large distances of  $\sim 1$  pc from where it was launched, the structure of the jet body is still quite inhomogeneous on small size scales of  $\lesssim 10^{15}$  cm. Thinner filaments produce the same flux in a smaller area on the sky (compared to fuzzy structures in ground-based images), so they have higher surface brightness,  $I_{H\alpha}$ , and they also have a smaller emitting layer thickness  $L$  along the line of sight. When deriving the electron density from the emission measure (see section 5), we have  $n_e \propto (I_{H\alpha}/L)^{1/2}$ , so the narrower structures imply higher electron densities. This is

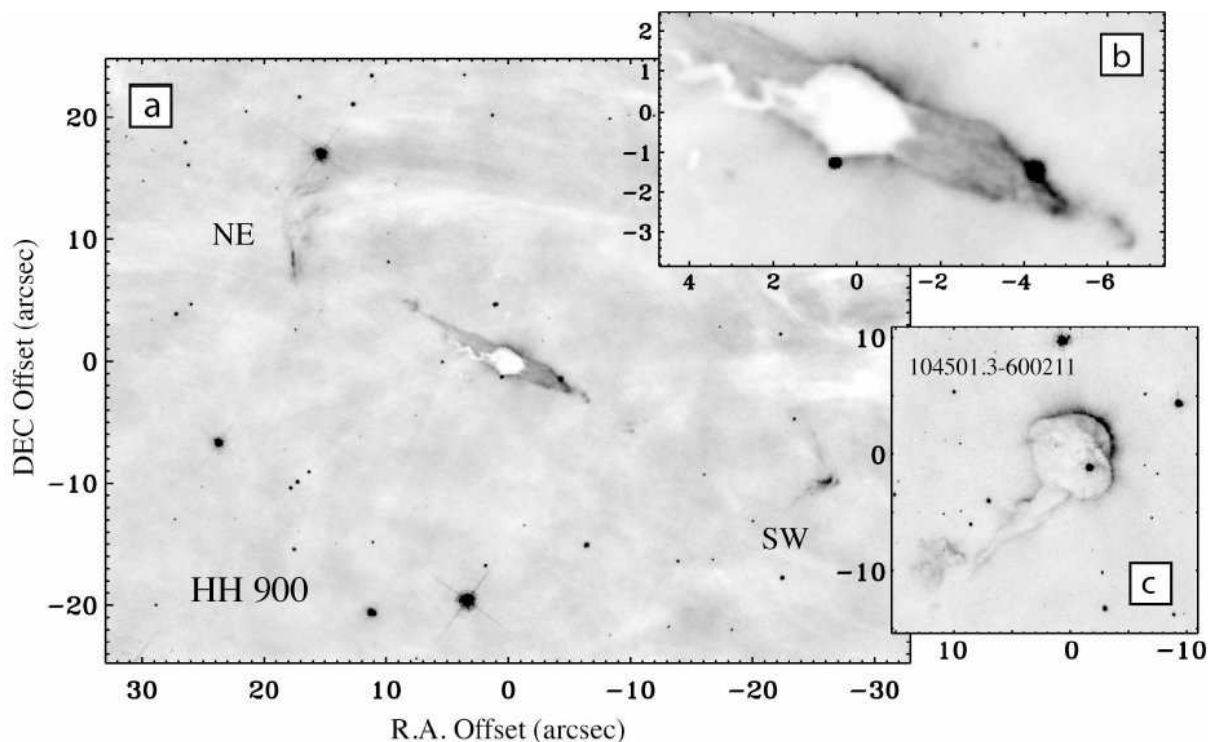


**Figure 4.** (a)  $H\alpha$  image of the bipolar jet HH 900 near Tr 16 (see Fig. 2). North is up and east is to the left. (b) A detail of the inner region of the jet and globule. (c) A different small tadpole-shaped dark globule (104501.3-600211; Smith et al. 2003) near Tr14 that does not show evidence for a jet.

important, because it resolves a discrepancy from our previous study (Smith et al. 2004c) where electron densities derived from the  $H\alpha$  emission measure were systematically lower by factors of 2–3 than electron densities from spectral diagnostics like the red  $[S\ II]$  doublet ratio, primarily because the individual filaments were not fully resolved.

### 3.2.2 HH 900

HH 900, shown in Figure 4a, is a stunning object. This bipolar jet explodes from a tiny ( $\sim 1''$  diameter) dark globule that was one of the original proplyd candidates seen in ground-based images of Carina (Smith et al. 2003). It resides within the bright inner region of NGC 3372 in Tr 16, but near the edge of the dark molecular ridge that bisects the Carina Nebula (see Figure 2). It is found only 2–3 pc from  $\eta$  Carinae and several massive O-type stars in the Tr 16 cluster, so the jet material outside the globule is bathed in a strong UV radiation field.

The morphology revealed in *HST* images is quite unusual. The small dark globule has a wiggly dark tail extending to the east, with peculiar and very angular kinks that make it look like a swimming tadpole or spermatozoon. On larger scales, one can see qualitatively similar wiggles in the tails of cometary clouds or in thin cords connecting the heads of dust pillars to a more distant clouds throughout Carina, as in HH 901 and HH 1008 (see below). The origin of these wiggles is unclear; they may arise from hydrodynamic instabilities as these cometary clouds are shocked and ablated (e.g., Pittard et al. 2009; Marcolini et al. 2005; Klein et al.

1994), or they may point to time-variable radiation fields in the region. An alternative explanation in the case of HH 900 is that two competing effects influence the strange tail morphology. On the one hand, the cometary tail pointing to the east must have been formed as a result of strong UV radiation or winds from the massive Tr 16 stars 2–3 pc to the west (from the right in Figure 4).<sup>2</sup> On the other hand, HH 900 is even closer ( $\sim 0.5$  pc) to the edge of a dark molecular ridge (see Figure 2), which appears as a very bright edge-on PDR at IR wavelengths (Smith et al. 2000; Smith & Brooks 2007). This PDR probably has a strong photoevaporative flow from the illuminated surface of the cloud, and this flow would form a pervasive westerly wind in the vicinity of HH 900. This photoevaporative wind may counteract the UV radiation force, and may act to compress the tail. Hydrodynamic models of such a scenario would be interesting. This same photoevaporative wind may also be needed to explain the jet bend toward the massive stars discussed below.

The bipolar jet emerging from the head of this tiny globule shows bright emission from both the main body of its collimated jet and from a pair of bow shocks at the ends of the flow. The full extent of the jet is about  $41''$  between the two bow shocks, or 0.46 pc, with the flow axis along  $P.A. \sim 242^\circ$ . The line connecting the apexes of the two bow shocks, however, passes about  $3''$  NW of the dark globule from which the jet emerges, indicating that the jet flow axis

<sup>2</sup> Note, however, that HH 900's tail does not point exactly away from  $\eta$  Car itself, which is to the northwest (upper right) in Figure 4, rather than due west.



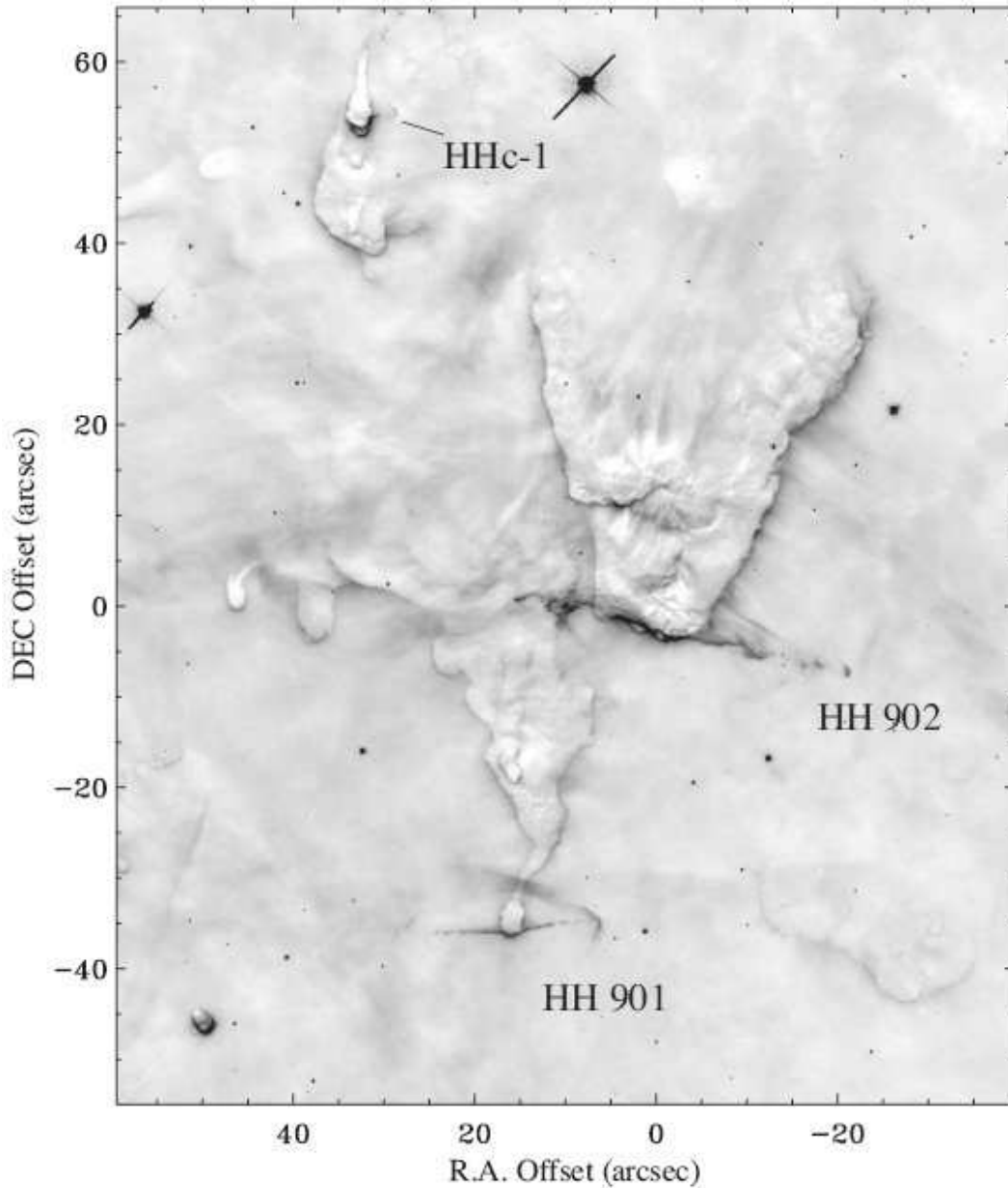


**Figure 5.**  $H\alpha$  image of the field including the two bipolar jets HH 901 and HH 902, north of Tr 14 (the Tr 14 cluster is located to the south, off the bottom of this figure). The jet candidate HHc-1 is also included in the field. North is up and east is to the left, and the offsets are relative to an arbitrary point near the origin of the HH 902 jet.

has been bent. Interestingly, however, the jet ends are bent *toward* the direction of Tr 16, rather than away from it as one would expect if the jet were bent by radiation pressure, the rocket effect, or a side wind as in LL Ori objects (see Bally et al. 2006). Bally & Reipurth (2001) noted several jets in NGC 1333 that bent toward the center of star formation activity as well, but in those cases this was thought to result because their driving protostars were dynamically ejected from the cluster. This is not the case for HH 900, where the cometary tail points in the wrong direction.

The fact that the dark tail is seen in silhouette in front of the eastern part of the jet suggests that the eastern flow is redshifted and the western flow is blueshifted; Doppler

velocities from spectra are not yet available to confirm this conjecture. The morphology in the pair of bow shocks conforms to the bow shock and Mach disk morphology typically seen in the terminal shocks of HH jets. The morphology of the collimated jet body, however, is somewhat bizarre and difficult to understand.

Zooming-in on the point where the western part of the jet flow first emerges from the dark globule, one can see remarkable structure, shown in the detail panel of Figure 4b. The jet body is quite wide, with 3-pronged elongated filaments seen in absorption. The central dark filament may correspond to dust entrained in the narrow body of the collimated jet itself seen in silhouette against the bright screen

of the background H II region. The two remaining dark filaments may be limb-darkened by dust in the side walls of the flow cavity, pushed aside and entrained as the jet cocoon exits the globule. Similar structures were seen in HH 280 in L1451 at the point where it first breaks out of its natal globule (Walawender et al. 2004).

About  $4''.5$  west from the center of the dark globule, along the jet body, there is a star that draws attention to itself (Figure 4b). It resides precisely at the center of a straight  $2''.5$ -long H $\alpha$  emission filament oriented at P.A. $\simeq 45^\circ$ , and the ends of this filament meet the boundary of the western part of the HH 900 jet. Is this simply a chance superposition of this star along the straight filament, or is this filament actually a bipolar microjet originating from that star? If the former is true, then it is unclear why the wide jet body appears to recollimate and then coincidentally end at the position of the star and putative microjet. If the latter is correct, then the morphological relationship between this putative microjet and the rest of the outflow gives the impression that this star and its associated outflow have recently been dynamically ejected from the dark globule. Although the image is intriguing, such conjecture is quite speculative without detailed spectroscopic information to provide kinematics of the star and jet material.

The HH 900 jet is significant in a broader context as well, because it confirms that even the smallest ( $\sim 1''$ ) dark globules in the interior of the H II region can harbor actively-accreting protostars, and that these dark globules are still important sites of active star formation within evolving H II regions. Many small dark globules without associated HH jets, such as the object in Figure 4c, may not be caught in this brief active outflow phase but may nevertheless harbor young stars or protostars. In such close proximity to  $\eta$  Carinae, HH 900 may — in the not-too-distant future — be polluted by nuclear-processed ejecta when that star dies in a violent supernova explosion. In that sense, the star that drives HH 900 provides an observed example of precisely the sort of conditions adopted in the models of Boss et al. (2008), where SN ejecta collide with a small cloud, imparting radioactive nuclides. These, in turn, are presumably then incorporated into chondrites within  $10^6$  yr after the SN, when the cloud material collapses into a disk, as is thought to have occurred in our Solar System. With a diameter of  $\sim 2''$  ( $\lesssim 10^{17}$  cm), the head of the dark globule is about half the *initial* size of the  $\sim 1 M_\odot$  cloud in the simulation discussed by Boss et al. (2008). At a distance of 2–3 pc from  $\eta$  Car, the dark globule has a cross section that would intercept a fraction  $\sim 10^{-5}$  of  $\eta$  Car's SN ejecta, if it were to explode. Thus, if  $\eta$  Car ejects at least  $10 M_\odot$  of processed ejecta in the explosion, then HH 900 would intercept  $10^{-4} M_\odot$  of SN material, comparable to the amount required to account for the inferred  $^{36}\text{Al}$  and  $^{60}\text{Fe}$  abundance in the Solar nebula (e.g., Foster & Boss 1997). HH 900, then, provides a glimpse of a young accreting protostar in the specific sort of environment where the Sun may have formed.

### 3.2.3 HH 901 and HH 902

The pair of outflows HH 901 and HH 902 are spectacular examples of irradiated bipolar jets (Figure 5).<sup>3</sup> They are extremely bright, and in hindsight, they can be seen on high-quality optical ground-based images. Unambiguous recognition of these features as jets, however, required the angular resolution of *HST*. Their high surface brightness of  $(2\text{--}6) \times 10^{-14}$  erg s $^{-1}$  cm $^{-2}$  arcsec $^{-2}$  is due to high jet densities and strong UV irradiation by Tr 14, located only  $\sim 1'$  (0.7 pc) to the south. The pillars from which HH 901 and 902 emerge do not point exactly at Tr 14, however. Instead, their axes point between Tr 14 and the massive O stars HD 93160/93161, thought to be members of Tr 16 (the bright pair of stars  $\sim 2'$  SE of Tr 14; see Walborn 2009).

HH 901 emerges from within  $\sim 1''$  ( $3 \times 10^{16}$  cm) of the very tip of a dark cometary dust cloud that is almost cut off from its natal dust pillar, with only a thin twisted cord connecting them. It is likely that it will soon appear as a bipolar jet from an isolated tiny cometary cloud, much like HH 900. HH 902, on the other hand, emerges from the tip of a thick dust pillar that is still solidly connected to its parent cloud. Several other cometary clouds without jets can be seen in the region, as well as one candidate bipolar jet from a tiny cloud (HHc-1, located in the upper left of Figure 5, and discussed more below).

The well-defined jet body of HH 901 extends to  $\pm 8''$  (0.09 pc) on either side of the globule, consisting of a highly collimated chain of H $\alpha$ -emitting knots implicating a time-variable outflow. Detailed inspection of the images shows that the jet body has a higher surface brightness on its southern edge facing Tr 14. The average orientation of the bipolar flow is along P.A. $\simeq 95^\circ$  ( $275^\circ$ ), although there is a slight bend in the jet, such that the eastern portion runs along P.A. $\simeq 92^\circ$ , while the western side is angled at P.A. $\simeq 279^\circ$ , although this may be partly due to the non-uniform illumination. The outflow terminates in a pair of parabolic bow shocks to the east and west (although the western bow is more clearly defined), marking a total end-to-end length of the outflow of  $\sim 23''$  (0.26 pc).

HH 902 is similar, oriented at P.A. $\simeq 258^\circ$ , with total jet length of over  $38''$  (0.42 pc). It also shows clear bow shock structures at its ends, although the structure along the jet is more chaotic than HH 901. It has a chain of dense knots, suggestive of variable outflow, with several twists and turns that implicate shaping by sideward radiation pressure, the rocket effect, or winds from the OB stars below in Tr 14. If the driving source were located halfway along the jet, it would reside within a curved protrusion in the dark dust pillar (an R.A. offset of  $-2''$  in Figure 5). HH 902's dust pillar has a strong photoevaporative flow normal to the pillar surface, through which HH 902 must burrow.

Like many jets studied here, the orientations of HH 901 and HH 902 are such that their outflow axes run roughly perpendicular to the axis of symmetry in their parent cometary cloud or dust pillar. Because they are extraordinarily bright and their bipolar jet structure is well-defined, we pursue a

<sup>3</sup> These were included in the large mosaic shown in Figure 2, and color images of HH 901 and HH 902 can be found at <http://heritage.stsci.edu>.

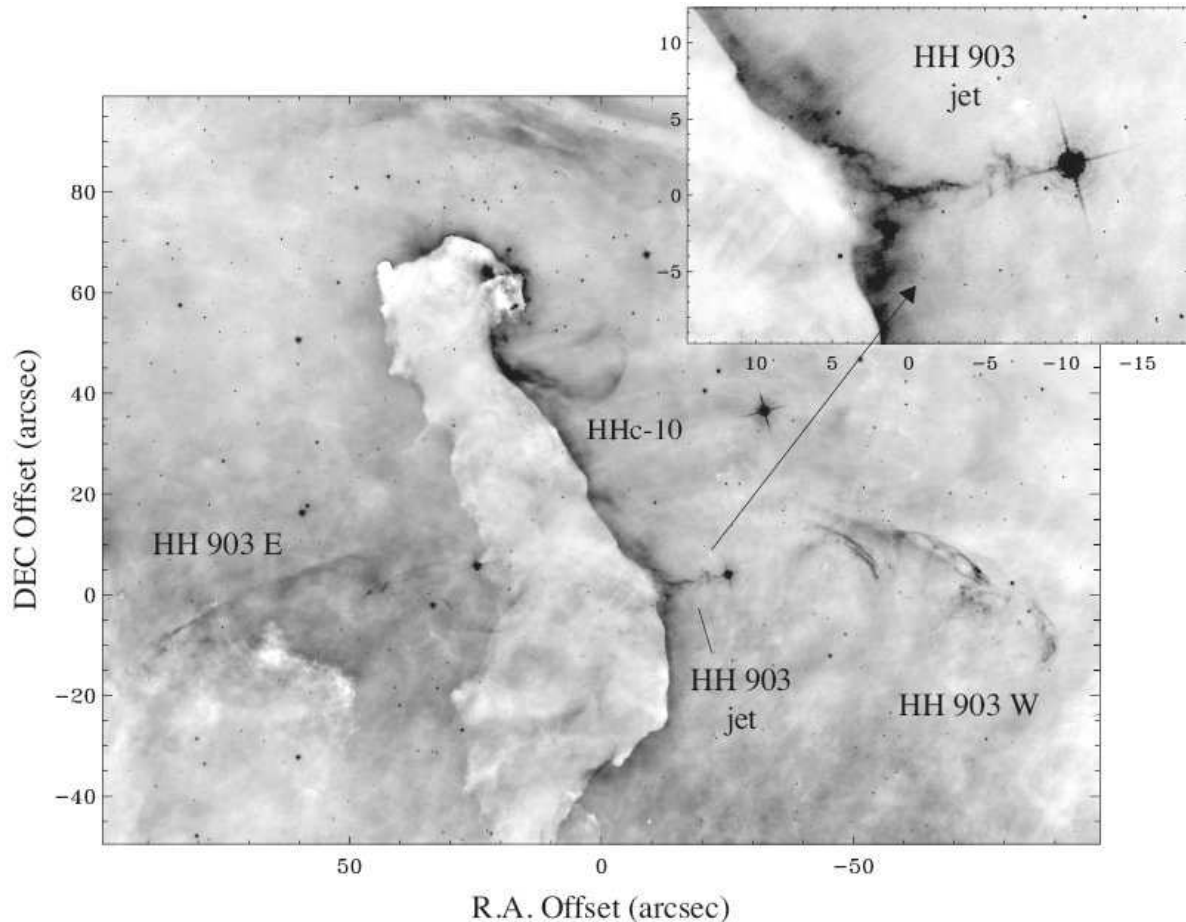


**Figure 6.** ACS H $\alpha$  image of the large dust pillar (G287.88-0.93) in the South Pillars of Carina. The field contains the parsec-scale bipolar outflow HH 903, which flows east and west to either side of the middle of the pillar and is over 2 pc in length. The field also contains the candidate jet HHc-10 associated with the pillar head (discussed later). North is up and east is to the left.

more detailed and more quantitative case study of the properties of these two jets in §4.

### 3.2.4 HH 903

HH 903 is a remarkable bipolar jet in the South Pillars that emerges from the sides of a large dust pillar (G287.88-0.93), shown in Figure 6. This pillar marks the relatively narrow top of an even larger structure that is the most massive concentration of molecular gas in the region, known as the “Giant Pillar” (G287.93-0.99; Smith et al. 2000), both of which point roughly toward  $\eta$  Carinae. HH 903 is an east/west flow oriented roughly along P.A.  $\approx 278^\circ$ , with a total length of about  $180''$  (2 pc). It is therefore among the longest protostellar outflows known, in the elite class of parsec-scale outflows (e.g., Bally & Devine 1994; Devine et al. 1997; Eislöffel & Mundt 1997; Marti et al. 1993; Ogura 1995; Poetzels et al. 1989; Reipurth et al. 1997b; Smith et al. 2004c).

We identify three main components to the HH 903 flow: the large bow shock structures to the east and west, HH 903 E and HH 903 W, respectively, and the main body of the jet (see Fig. 6). The bow shocks are asymmetric, with their curved shock structures appearing much brighter on their northern sides. If these two bow shocks are density

enhancements along parabolic cones, their “top-lighted” appearance in Figure 6 probably arises because they are illuminated from above by OB stars in Tr 16 far to the north. This suggests that the southern surfaces of the bow shocks are partly shielded because neutral gas within them or at their northern surfaces absorbs most of the ionizing radiation. Alternatively, the northern parts of HH 903E and 903W may be brighter because of higher density, having been compressed by the ram pressure of the large-scale flow of plasma descending from above in Figure 6.

The jet body of HH 903 erupts from the western side of the dust pillar, with a chaotic stream of condensations about  $12''$  (0.13 pc) in length. Since the detectable jet body terminates long before reaching the bow shock, it suggests that the HH 903 flow has been intermittent.

HH 903 is similar to many other jets in Carina in that its axis appears to be roughly perpendicular to the axis of the elongated dust pillar or cometary cloud from which it emerges, but it is unusual in that the driving source is not located at the apex of the dust pillar. Instead, the driving source is located halfway down the dust pillar. Judging from the collimated morphology of the jet, its driving source is likely to be close to the west ionization front.

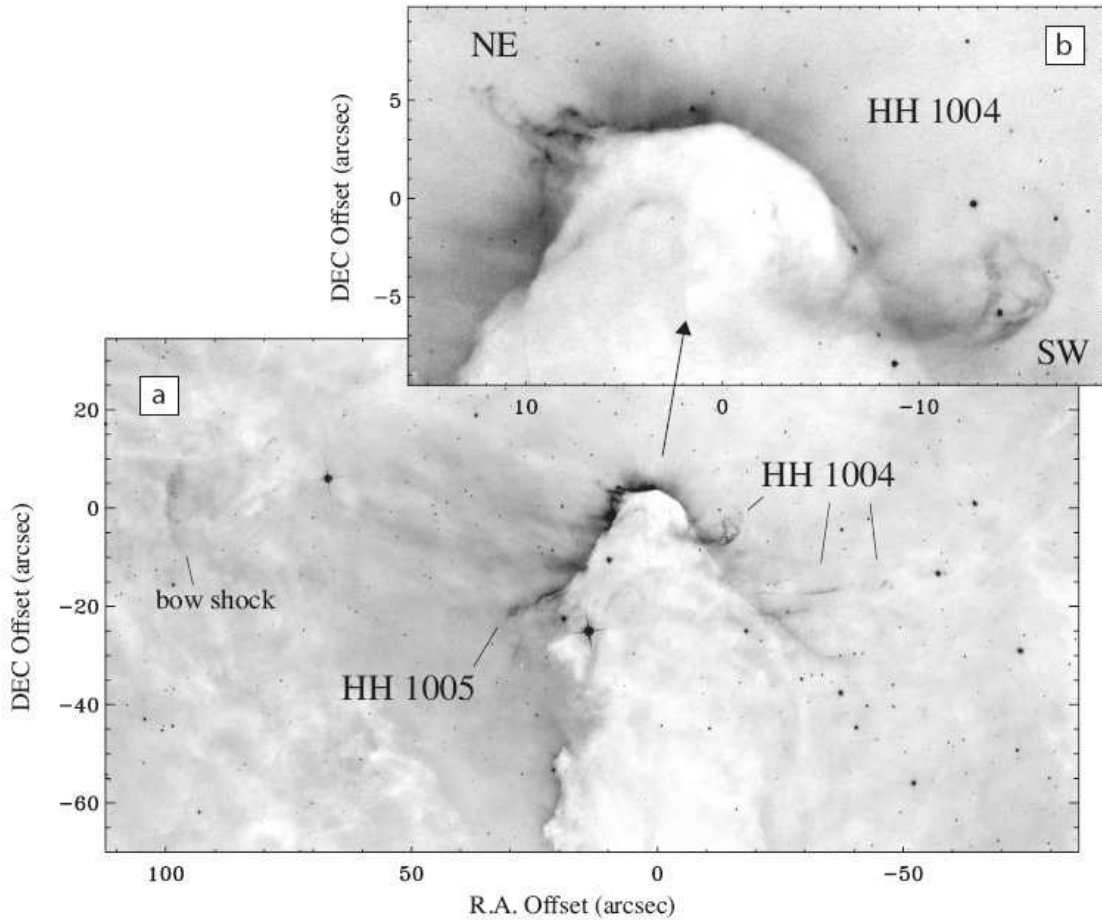


**Figure 7.**  $H\alpha$  image of the tip of another large dust pillar in the South Pillars, which contains the bipolar jet HH 1004 closest to the tip of the pillar, and the one-sided jet HH 1005, which appears to be a separate flow. There is also a large bow shock at left, probably associated with HH 1004.

### 3.2.5 HH 1004 and HH 1005

The two outflows HH 1004 and HH 1005 both emerge from the head of the same dark cloud in the South Pillars, and both are shown in Figure 7a. This is one of the more prominent dust pillars in the region, but it has not been discussed before in the literature. Like its cousins, the pillar points north in the general direction of Tr 16, although its symmetry axis actually points  $\sim 15^\circ$  east of  $\eta$  Car.

HH 1004 is clearly a bipolar jet with flows seen emerging to the NE and SW from the very tip of the dark pillar in Figure 7b. HH 1004 NE has a somewhat chaotic structure, perhaps arising as it plows through a dense photoevaporative flow. HH 1004 SW has a large and more well-defined bow shock structure that is brighter on its southern side, opposite the direction facing the ionizing stars but toward the denser photoevaporative flow. The full length of the inner part of HH 1004's bipolar jet is roughly  $32''$  (0.36 pc), with its axis along  $P.A. \simeq 247^\circ$ . However, there also appear to be more distant shock structures associated with the HH 1004 flow. Continuing to the southwest from the bow-shock structure HH 1004 SW noted above, there are several curved filaments along the same axis (identified in Figure 7a) that probably represent a more distant terminal shock along the same flow. Similarly, far to the east there is a large bow shock struc-

ture, which is labeled in Figure 7a. This bow shock is not along the presumed axis of HH 1004, but it seems likely that this is a distant bow shock in a curved flow that is part of HH 1004 rather than HH 1005, because HH 1005 points in an altogether different direction. Including these distant shock structures, the total length of the HH 1004 jet is roughly  $150''$  (1.7 pc), placing it among the longest parsec-scale HH jets known.

HH 1005 emerges from the tip of the same dust pillar, but only one side of the flow is seen, directed in the SE direction. In HH 1005,  $H\alpha$  emission traces a collimated jet body, but no distant bow shocks are seen along a projection of the same axis. The body of this jet is likely to be quite dense, because its northern face is much brighter, suggesting that the jet body is optically thick to ionizing photons, which therefore cannot penetrate all the way through it (as is the case for clearer examples such as HH 901 and 902, or jets in Orion discussed by Bally et al. 2006). The length of the emitting portion of the jet that we detect is roughly  $15''$  (0.17 pc), with an axis along  $P.A. \simeq 112^\circ$ . Projecting this axis into the cloud, the IR driving source should be located a few arcseconds south of HH 1004's protostar.

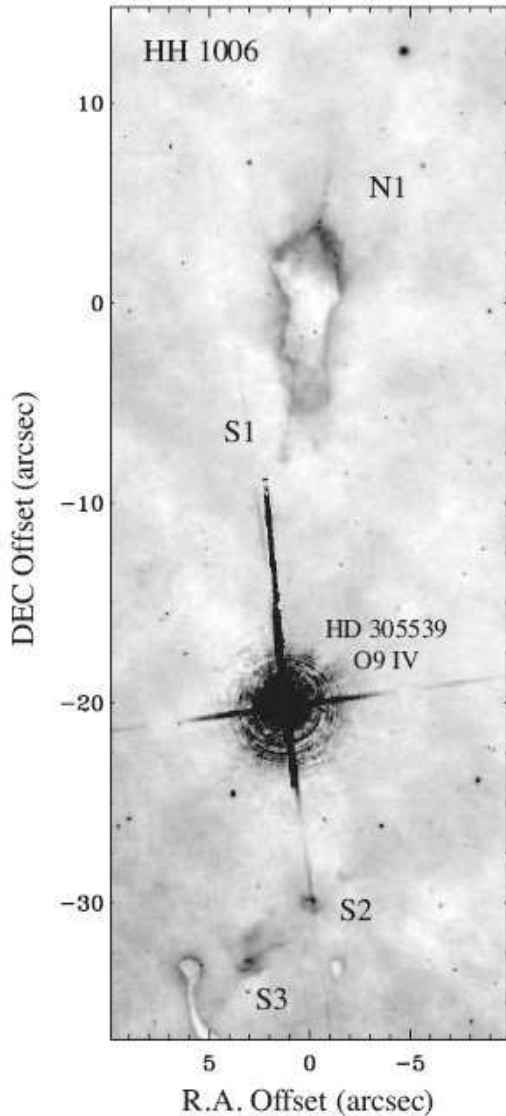


**Figure 8.** ACS  $H\alpha$  image of the highly collimated bipolar jet HH 1006, emerging from a dark cometary globule. The north (N1) and south (S1) parts of the collimated bipolar jet flow are identified, as well as two more distant shock structures to the south (S2 and S3) that are probably part of the same outflow. The bright star in the center is the O9 IV star HD 305539.

### 3.2.6 HH 1006

HH 1006, shown in Figure 8, is a narrow and straight collimated bipolar jet. It emerges from an embedded star inside a dark cometary globule that is one of the proplyd candidates from Smith et al. (2003), although here it resembles a bright-rimmed cometary cloud rather than Orion’s proplyds. The putative embedded star is not detected in our ACS  $H\alpha$  image due to extinction within the cloud. The small cometary globule is located amid the South Pillars, and it points north toward  $\eta$  Carinae.

The narrow HH 1006 jet is a chain of faint knots, stretching over a full jet length of roughly  $16''$  (0.18 pc). The jet points along roughly the same axis as the globule, and the bipolar jet does not deviate from its axis by more

than about  $1^\circ$ . Farther south one sees two additional shocks, likely to be distant terminal shocks in the same outflow, denoted S2 and S3 in Figure 8. Including these, the total length of HH 1006 is  $\sim 40''$ , or over 0.45 pc. The bright O9 IV star HD 305539 is seen along the southern jet axis, but this may be a chance alignment.

### 3.2.7 HH 1007 and HH 1015

HH 1007 in Figure 9 is a dense collimated jet body associated with a small complex of dark clouds in the far southern region of the South Pillars (Pos. 25 in Fig. 1). The overlapping cometary clouds in this dark cloud complex all point north toward  $\eta$  Carinae, Tr 16, and Tr 14. A large curved structure may indicate a bow shock, but the morphology is complicated because the jet appears to be impacting another cloud or plowing through its dense photoevaporative flow. The jet projects eastward to the left-most of the dark clouds in Figure 9, suggesting that this is the location of its driving source. The observed jet length is roughly  $8''$  (0.09 pc) running roughly due west at P.A.  $\sim 270^\circ$ .

HH 1015, also shown in Figure 9, is a chain of very faint but well-collimated emission knots that is  $\sim 6''$  (0.07 pc) long, with its axis at P.A.  $\sim 315^\circ$ . It is a one-sided jet emerging to the northwest from the head of a dark cometary cloud, and appears similar to HHc-5 and HH 1014. The dark globule from which HH 1015 emerges is part of the same complex of overlapping cometary clouds that launches HH 1007.

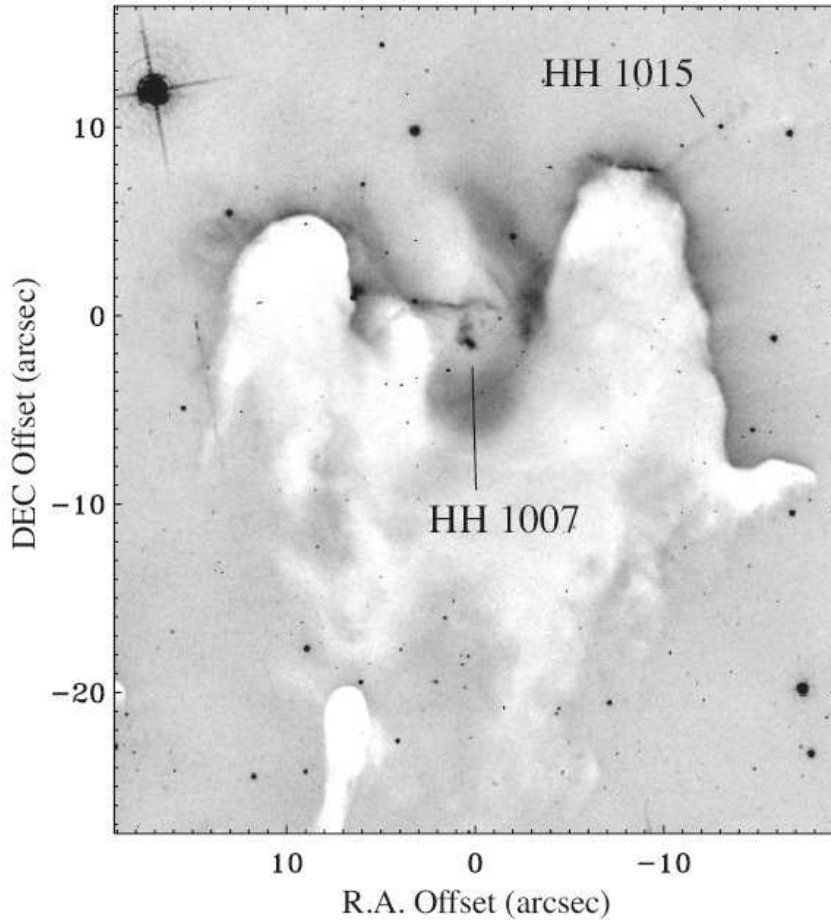
### 3.2.8 HH 1008

Figure 10 shows the field around HH 1008, which is a giant and elegant bow shock structure spanning more than  $45''$  (0.5 pc). The  $H\alpha$  image also shows a dense knot at the apex of the parabolic shock, which is likely to be its Mach disk where the collimated jet is decelerated, although the jet body itself is not detected.

The long, thin, and twisted dark cloud in Figure 10 is G287.73-0.92, which terminates with a bright tadpole-shaped cometary cloud that points north to  $\eta$  Carinae. Although the *HST*  $H\alpha$  image does not reveal a collimated jet body associated with HH 1008, the parabolic bow shock has an axis of symmetry that points north along its open end, up toward this cometary cloud, so this is the most likely location of its driving source. Indeed, there is a partially obscured star at the apex of this cometary cloud that is seen in the  $H\alpha$  image. If this is the driving source, then the southern flow in HH 1008 has a length of roughly  $105''$  (1.2 pc). The candidate flow HHc-2 emerges to the north from this source, and it may be the counter-flow to HH 1008.

### 3.2.9 HH 1009

HH 1009 is an unusual case, seen in Figure 11. The dense filaments are distinct from other wisps and filaments in the background H II region, and their morphology clearly resembles shock structures in HH jets. (In this sense it is similar to HH 1007, discussed above.) One can see thin bow shocks surrounding clumps of emission that are probably Mach disks or other working surfaces in the flow. However, images do not reveal a collimated jet body, so it is unclear exactly



**Figure 9.** ACS H $\alpha$  image of a dark globule amid the South Pillars in Carina (Pos. 25 in Figure 1), containing the rather mangled one-sided jet HH 1007 (center) discussed in §3.2.7, as well as the collimated jet HH 1015 (upper right) also discussed in §3.2.7.

where the jet originates. Its likely origin is within the base of the large dark dust pillar to its west, which is the base of the pillar associated with HH 1008.

### 3.2.10 HH 1010

HH 1010 is a highly collimated bipolar jet emerging from the very tip of a large and dark dust pillar at the western edge of the southern Carina Nebula (Figure 12). It is associated with the large edge-on western ionization front in the southern polar lobe of the nebula; see Smith et al. (2000). The symmetric parts of the inner bipolar jet extend  $\pm 15''$  to the northeast (NE) and southwest (SW) from the presumed driving source at the head of the jet. However, additional shock structures along the same axis are seen farther to the southwest (a possible bow shock is marked as HH 1010 A in Fig. 12), making the full length of the jet at least  $60''$  ( $0.7$  pc) along roughly P.A.  $\approx 216^\circ$ . With the driving source located along the jet axis inside the dark dust pillar, the driving source must be within  $\sim 2''.5$  ( $\lesssim 10^{17}$  cm) from the ionization front. There is a faint optical point source within the boundaries of the dark pillar and along the jet axis closer to the NE part of the flow, but it is not clear yet if this is actually the driving source.

This jet provides an illustrative and striking example of

what seems to be a fairly common phenomenon – collimated bipolar jets that emerge from the heads of dust pillars, with an axis orientation roughly perpendicular to the long axis of the parent dust pillar or cometary cloud. Several examples are seen in our study of Carina (HH 666, 900, 901, 902, 1004, HHc-1, etc.), although some counter examples also exist where the jet emerges at apparently random angles (e.g., HH 1011, 1013, 1014, HHc-5). Another good example of a jet perpendicular to its cometary globule outside Carina is the remarkable jet system in L1451 in Perseus, consisting of the chain of HH objects HH 280, 317, 492, and 493 (Walawender et al. 2004). This is discussed further in §6.3. The large dark dust pillar from which HH 1010 emerges points eastward, in the general direction of  $\eta$  Car, Tr 16, and the upper parts of Cr 228 (see Smith 2006; Walborn 2002), as do neighboring cometary globules to the south in Figure 12.

### 3.2.11 HH 1011

HH 1011, shown in Figure 13, is a one-sided jet that is only  $2''$  long ( $0.02$  pc). It emerges from a small cometary globule located near the Tr 15 cluster, but like a few dozen other small cometary clouds in the vicinity (not shown), the head of the cometary cloud points to the Tr 14 cluster. The H $\alpha$  images do not show clear evidence for a bow shock further



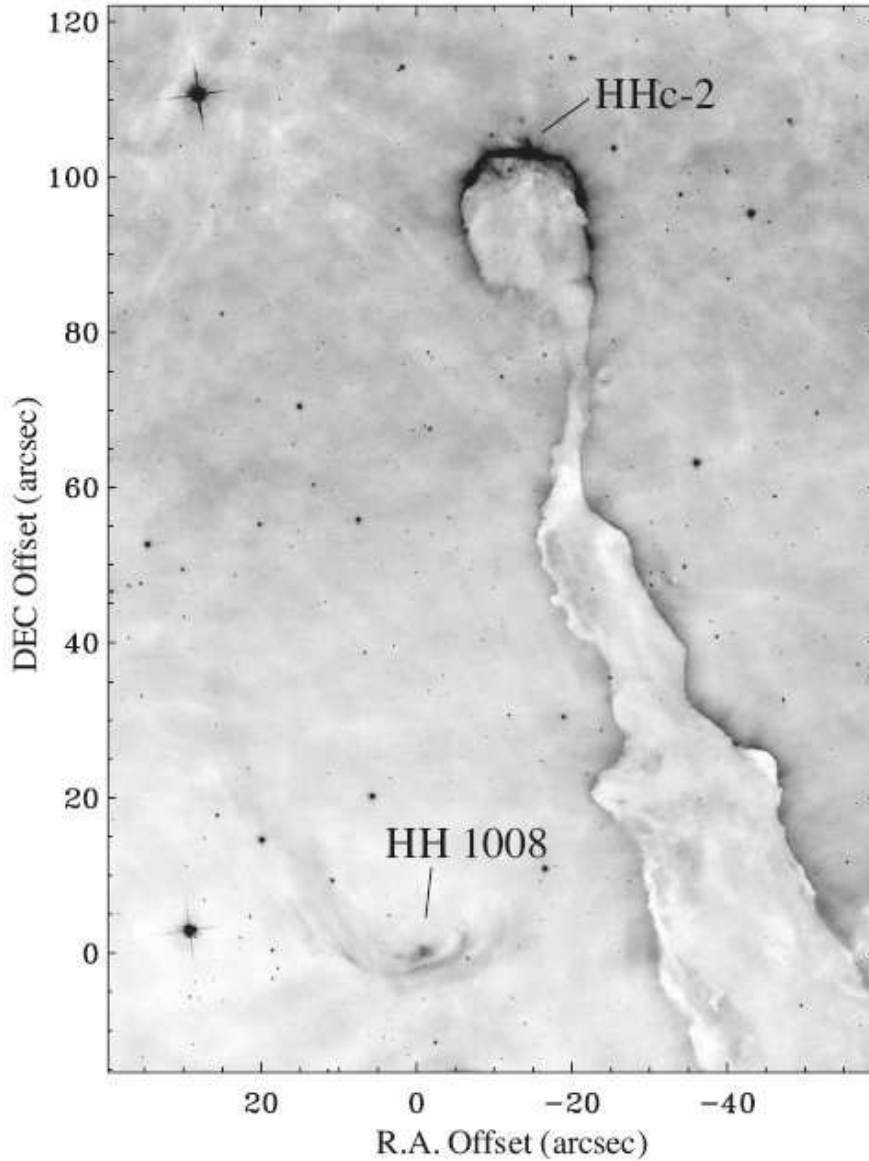


**Figure 10.**  $H\alpha$  image of the giant bow shock HH 1008, the wings of which stretch across roughly  $45''$  ( $0.5$  pc). The tadpole shaped structure is the tip of a long wiggly dust pillar associated with the cloud G287.73-0.92. Although no collimated jet body is seen, the driving source of the jet is clearly to the north of HH 1008 and may be located inside the head of this pillar. The candidate jet HHc-2 emerges from the north end of this same cometary cloud and may be the counter-jet in a bipolar flow.

along the jet axis, nor do they reveal any evidence for a counter-jet in the opposite direction.

### 3.2.12 HH 1012

HH 1012, shown in Figure 14, is a clear example of the class of “LL Orionis objects”, which exhibit parabolic or C-shaped shock fronts surrounding visible stars (see Bally & Reipurth 2001; Bally et al. 2001, 2006). These parabolic fronts tend to be associated with jets that are deflected by large-scale bulk flows of plasma away from the core of an H II region like Orion (Masciadri & Raga 2001), although the jet bending may also be caused by radiation pressure or the rocket effect if the jet core is neutral (Bally et al. 2006). In the case of HH 1012, the wings of the parabolic shock point away from

the Tr 14 cluster, located a few arcminutes southwest, which would be the dominant source of photons or a bulk flow from its collective stellar winds.

Bally et al. (2006) provided a detailed analysis of LL Ori objects and the kinematics of their jets, such as the exemplary case of HH 505 in Orion. HH 1012 has all the hallmark properties of Orion’s prototypical LL Ori objects like HH 505. There are clumps within the parabolic front that resemble internal working shocks in the jets of other LL Ori objects, and HH 1012 even appears to harbor a tiny  $0''.5$  ( $0.005$  pc) microjet from its central star, at P.A.  $\approx 140^\circ$ . The total length of the visible jet in HH 1012 is  $\sim 16''$  ( $0.18$  pc).

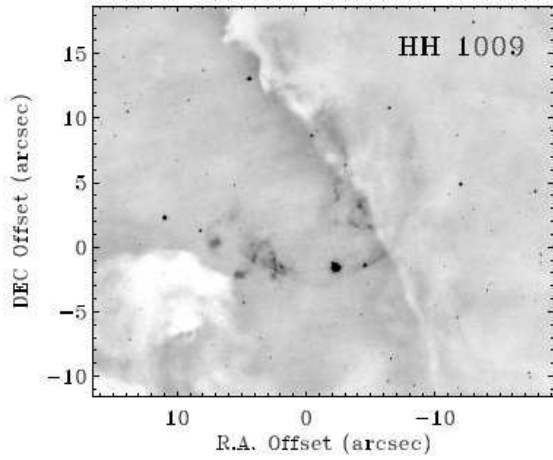


**Figure 11.**  $H\alpha$  image showing HH 1009, an outflow emerging from the side of the same pillar associated with HH 1008. This feature is located off the bottom of Figure 10.

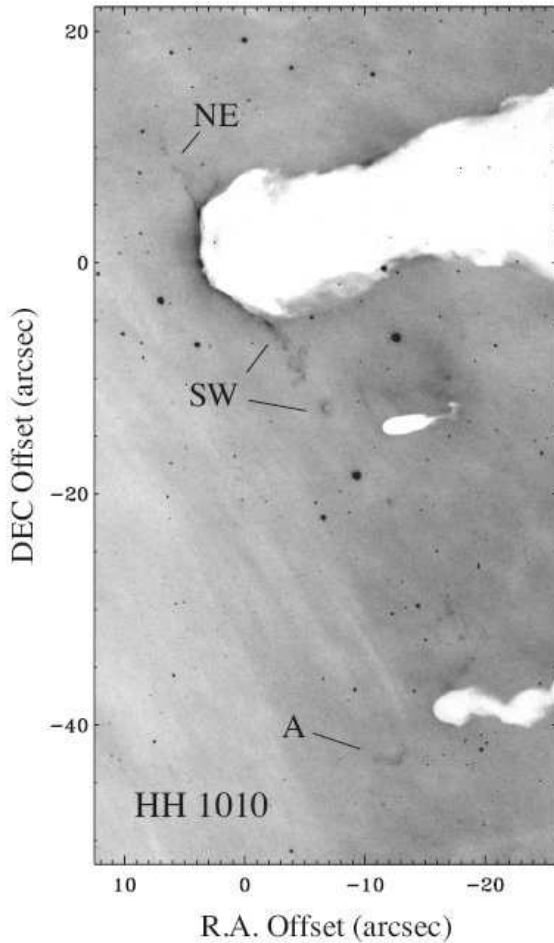


**Figure 12.**  $H\alpha$  image of HH 1010, a highly collimated bipolar jet emerging to the northeast (NE) and southwest (SW) from the very tip of a dust pillar near the western edge of Carina. Several internal shocks and a bow shock in the flow (A) can be seen.

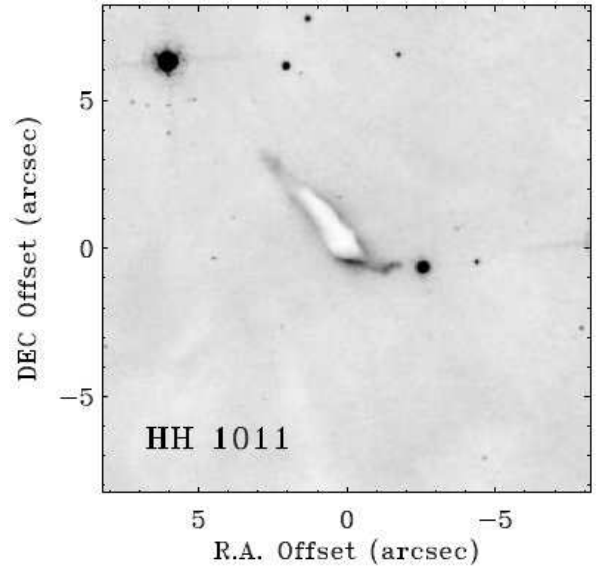


**Figure 13.** ACS/WFC  $H\alpha$  image of HH 1011, a microjet from a small dark cometary cloud located near Tr 15.

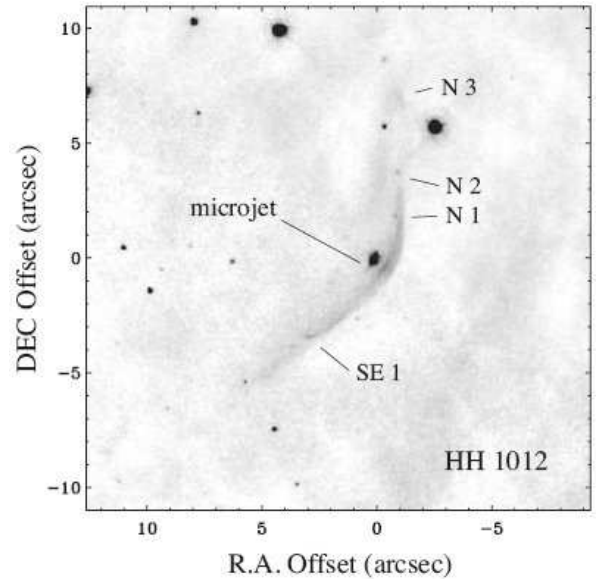


**Figure 14.** The LL Ori-like object HH 1012 in an  $H\alpha$  ACS image. In addition to the larger curved shock structure, one can see shocks within the jet and a tiny microjet from the central star.

### 3.2.13 HH 1013

The outflow HH 1013, shown in Figure 15, is an extremely long jet stretching over  $130''$  or almost 1.5 pc. The source of HH 1013 is a proplyd, found near the tip of a long and twisted cometary cloud structure that is perhaps in a more advanced stage of evaporation than the similarly twisted dust pillar near HH 1008. It is located near the Tr 14 cluster (see Fig. 2), and the long tail points away from Tr 14, which is located a few arcminutes to the south, off the bottom of Figure 15a. This elongated cloud was one of the long tail

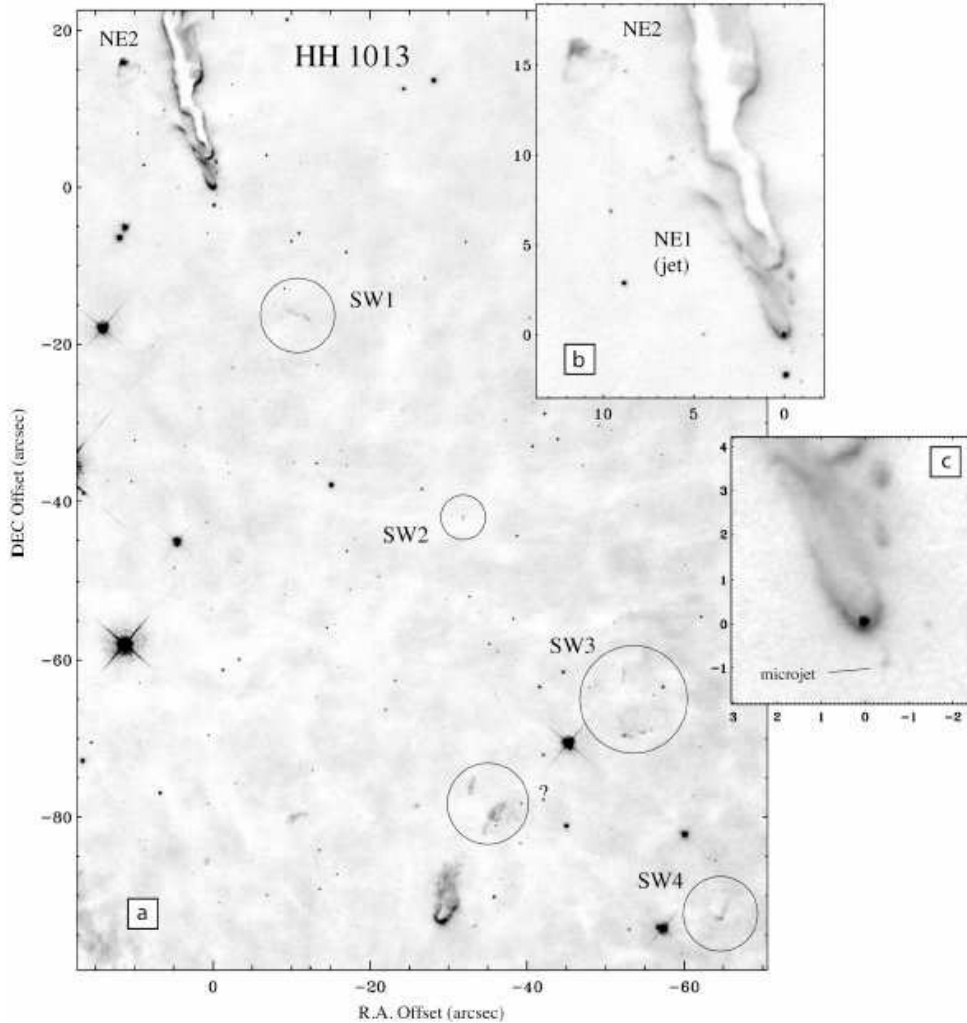


**Figure 15.** (a) This ACS H $\alpha$  image captures one of the long tail structures noted by Smith et al. (2003), and the long bipolar HH 1013 jet associated with it. The NE outflow of HH 1013 has a clear bow shock (NE2) and jet body (NE1) emerging from the bright central star in the proplyd at the southern end of the elongated cloud structure in the upper left. Several individual shocks in the flow can be seen far to the southwest (SW1-4). SW4 appears to be the terminal bow shock. The one circled feature marked with a "?" may be a bow shock as well, but it may also be an illuminated cloud like many of the other structures in the lower left portion of the image. (b) A detailed view of the proplyd at the end of the cloud, containing the star that is the likely driving source of HH 1013, as well as the NE flow. (c) An even more detailed view of the possible counter-jet emerging from the tip of the proplyd (labeled as "microjet").

structures found in ground-based images by Smith et al. (2003), along with several proplyd candidates.

HH 1013 is a bipolar jet that flows to the NE and SW from the proplyd located at (0'', 0'') in Figure 15. To the northeast it is comprised of a clear parabolic bow shock (HH 1013 NE2), and a collimated but meandering body of the jet (NE1), shown most clearly in Figure 15b. The detailed morphology of the parabolic bow shock HH 1013 NE2 resembles other well-studied examples of bow shocks with Mach disks, and is consistent with the jet direction implied by the collimated jet body to its lower right. The driving source of the jet is almost certainly the star within the proplyd at the head of the cometary cloud. The length of the north-east arm of the jet is  $\sim 21''$  (0.23 pc), with an axis at roughly P.A.  $\simeq 35^\circ$ . There appears to be a slight bend in the axis of the NE jet at 7–9'' from its origin, perhaps due to the influence of a photoevaporative flow off the side of

the elongated globule. In the opposite direction, a chain of shocks stretches  $\sim 110''$  (1.23 pc) to the southwest, labeled as SW1-4. SW4 is probably the terminal bow shock in the flow. Several other nebular features are seen in the field, in the lower left and center of Figure 15a, but upon close inspection most of these appear to be irradiated clouds.

The driving source of HH 1013 is significant, because it is an unambiguous example of a true analog of the proplyds in the Orion Nebula. Most structures that resemble the proplyds in Carina and other H II regions appear to be dark cometary clouds upon closer inspection. (Some of these nevertheless appear to contain embedded stars with active accretion and outflows, as described elsewhere in this paper.) A detail of this proplyd is shown in Figure 15b. Although we do not resolve a small dark silhouette disk inside the proplyd, its tadpole shape arises because of a proplyd outflow

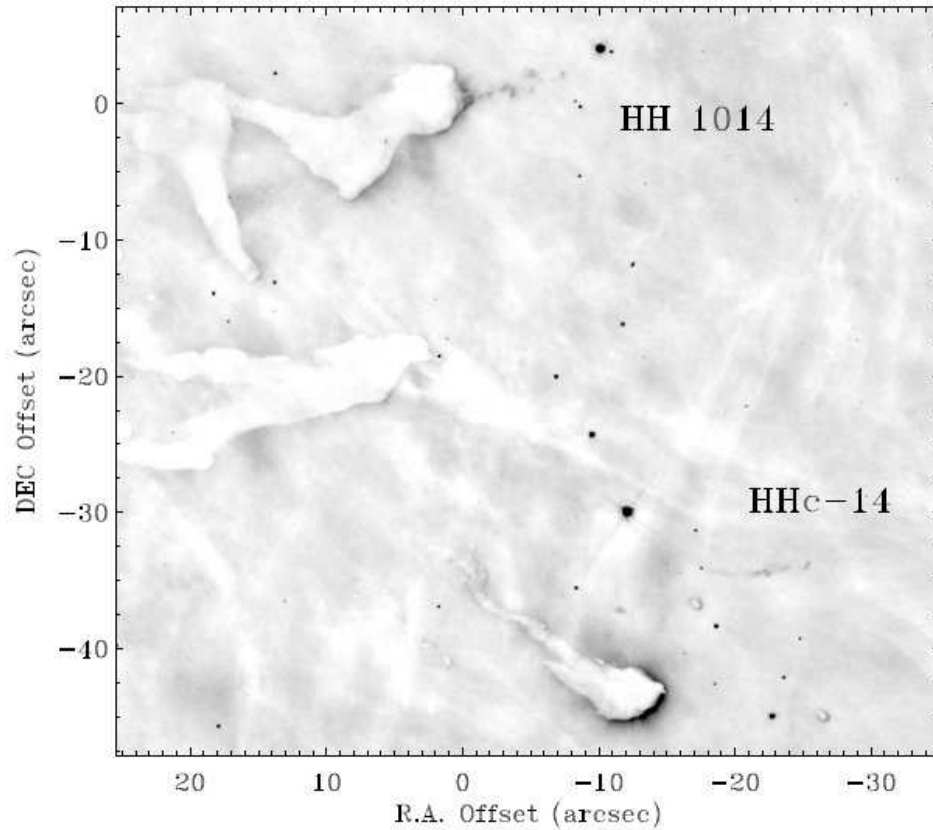


**Figure 16.** HH 1014, located at the eastern edge of the inner Carina nebula, is within the Tr 16 mosaic field and emerges to the NW from a small pillar head. The pillar head and the one-sided HH 1014 jet point roughly toward  $\eta$  Carinae and Tr 16. The candidate jet shocks labeled HHc-14 are also in the field to the lower right, but do not lie along the HH 1014 jet axis.

rather than a from an opaque cometary cloud, because the internal star is seen clearly.

Like many of Orion’s proplyds, this one associated with HH 1013 appears to have a tiny microjet only  $1''$  ( $\sim 0.01$ ) long, which protrudes from the head of the proplyd in the direction opposite from of the flow that terminates with HH 1013 NE2 (see Figure 15). This microjet is the start of the counterflow that produces the SW1–4 structures.

### 3.2.14 HH 1014

The one-sided jet HH 1014 is a collimated chain of emission knots emerging from the head of a dark globule, seen in the ACS/WFC H $\alpha$  image in Figure 16. These emission knots are likely photoionized condensations arising from internal working surfaces in the flow. No clear bow shock structure can be identified, nor do the images reveal any obvious counter-jet. No driving source is seen at visual wavelengths; it is probably embedded within the dark cloud.

The jet stretches roughly  $8''$  (0.09 pc) westward along P.A. $\simeq 290^\circ$ . This is only a few degrees different from the axis of the elongated dust pillar from which it emerges, and this is also roughly the direction toward  $\eta$  Carinae. HH 1014 is found at the eastern edge of the bright inner part of the Carina Nebula, within the Tr 16 mosaic (see Fig. 2) and along the dark molecular ridge not far from HH 900.  $\eta$  Car is located a few arcminutes to the right. The nearby shock

structure HHc-14 (Figure 16) is probably part of a different flow because it is not along the axis of HH 1014.

### 3.2.15 HH 1015

See §3.2.7.

### 3.2.16 HH 1016

HH 1016 (Figure 17) is a one sided jet about  $25''$  (0.3 pc) in length, emerging along P.A. $\simeq 320^\circ$  from the top of the dust pillar that harbors the Treasure Chest cluster (Smith et al. 2005c). The dust pillar is the most luminous mid-IR source in the South Pillars (Smith et al. 2000), while the Treasure Chest cluster itself is extremely young ( $\sim 10^5$  yr) with a very high YSO disk excess fraction (Smith et al. 2005). The embedded source that drives HH 1016 is probably a member of this young cluster. The counter jet is invisible, probably because it burrows into the dust pillar.

The bow shock of HH 1016 is seen in the upper right corner of Figure 17. It has clear parabolic bow-shock structure. The bright Mach disk at its apex also emits strong [Fe II]  $1.644 \mu\text{m}$  emission, which can be seen in hindsight in narrowband near-IR images (Smith et al. 2005c).

The driving source of the jet cannot be clearly seen, and there is no clear feature that one can attribute to the collimated inner jet of this flow. However, one can see bright fila-

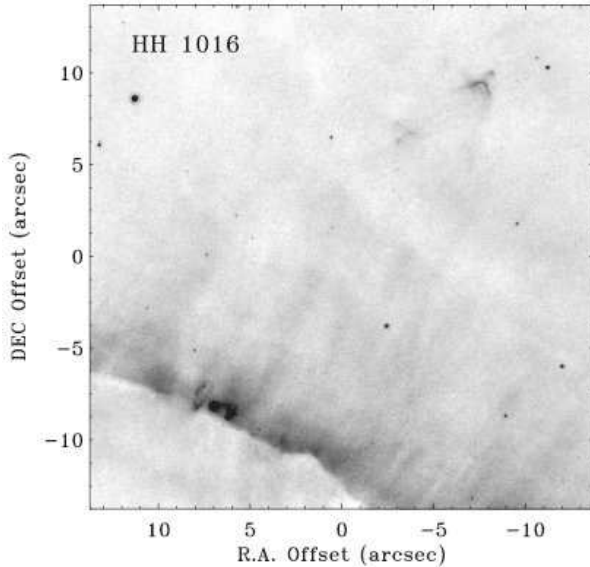


**Figure 17.** An  $H\alpha$  image of HH 1016, located about  $30''$  north of the Treasure Chest cluster (Smith et al. 2005c), and emerging from the top of the same dust pillar that contains the cluster. There is a parabolic bow shock in the upper right of this image, and one can see filaments in the lower left where the jet breaks out through the ionization front. The broad band of emission running diagonally through the image is the photoevaporative flow from the surface of the dust pillar.

ments of emission at the point where the jet breaks through the ionization front, at roughly  $(6'', -8'')$  and  $(8'', -7'')$  in Figure 17. These breakout filaments resemble similar features where other HH jets emerge from their embedded sources, as in HH 900, HH 903, HH 1003 A, HH 1004, HHc-2, etc. The two filaments are on either side of a faint star, which may or may not be the driving source of the outflow.

### 3.2.17 HH 1017

HH 1017, shown in Figure 18, is a bent bipolar jet located east of the Tr 14 cluster (see Figure 2). Tr 14 is located off the right side of Figure 18, and HH 1017 bends away from Tr 14, as one might expect of radiation and winds from the extreme O stars in Tr 14 are pushing the jet.

Unlike most HH jets we have found in Carina, HH 1017 does not emerge from an invisible source embedded deep within a dark dust pillar, but instead comes from an exposed star with no dark clouds nearby. A collimated jet body runs about  $4''$  (0.05 pc) to the southwest from this driving source, while several other bow shocks in the flow can be seen. These shocks trace out a gracefully bending jet with a full length over  $35''$  (0.4 pc). HH 1017 is reminiscent of several graceful bent jets in Orion, especially HH 502 (Bally et al. 2006). The average direction of the flow is  $P.A. \sim 25^\circ$ , but obviously the flow direction changes with distance from the source.

### 3.2.18 HH 1018

HH 1018 (Figure 19) is a microjet in the central Carina Nebula, located within the Tr 16 cluster not far from  $\eta$  Car and HH 900 (see Figure 2). Like HH 1017, the jet originates

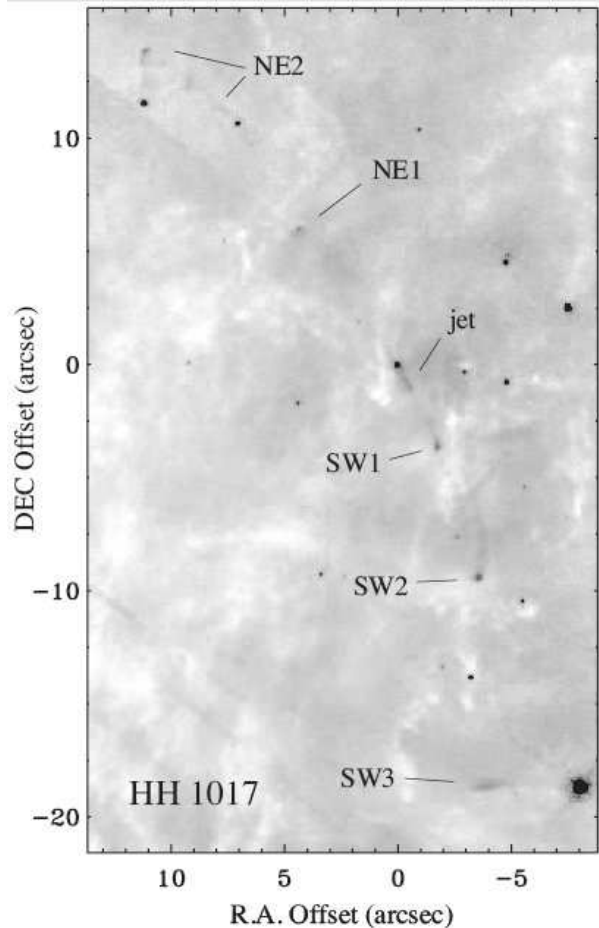


**Figure 18.** The long bent jet HH 1017 in  $H\alpha$ . The source of the jet is the star at (0,0). A collimated jet body is seen emanating from this star toward the south-west. Several shocks to the north-east and south-west can also be seen.

from an exposed star, although here there is a small dark globule projected nearby. HH 1018 is a one-sided jet, with no sign of features associated with a counter jet in a bipolar flow. The microjet is about  $2''$  (0.02 pc) long, but there is also an additional shock structure located  $\sim 10''$  (0.11 pc) along the same axis.

The central star and its microjet may resemble some proplyds at first glance. However, we have discounted this possibility, since the proplyd tail would point in the wrong direction, i.e. the proplyd tail should point *away* from the massive O-type stars in Tr 16, but it points *toward* them. This fact, combined with the additional emission knot along the same axis, argues that HH 1018 is a jet.

## 3.3 Jets in NGC 3324

We imaged a small portion of the adjacent H II region NGC 3324 at its sharp edge-on ionization front at the western side of the nebula using the  $H\alpha$  filter on ACS/WFC. Subsequently, the same region was imaged with *HST*/WFPC2 in the [O III]  $\lambda 5007$  F502N and [S II]  $\lambda \lambda 6717, 6731$  F673N filters by the *Hubble Heritage* team, and the resulting color

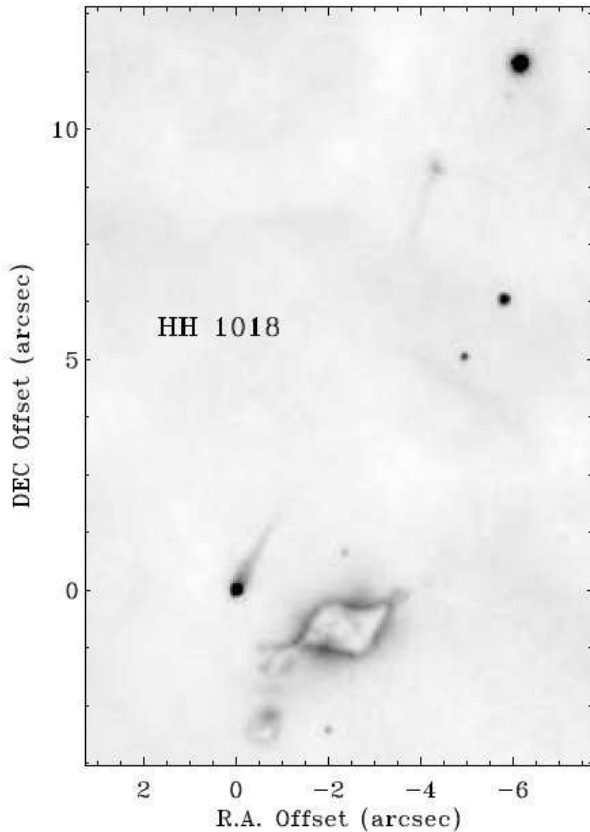


**Figure 19.** The microjet HH 1018 in  $H\alpha$ , located south of  $\eta$  Car in Tr 16. The source of the jet is the star at (0,0). A collimated jet body is seen emanating from this star. A shock structure farther along the same axis can also be seen.

image of the region is shown in Figure 20a.<sup>4</sup> The resulting data reveal multiple outflows based on their collimated or bow shock morphology and their high  $[S\ II]/H\alpha$  ratios. Two objects (HHc-1 and HHc-2) remain candidate jets, while another (HH 1003) has several parts that may be more than one outflow. In all three cases discussed below, the driving source is not identified at visual wavelengths.

### 3.3.1 HH 1002

Figure 20c shows HH 1002, which is an irradiated collimated jet about  $50''$  long ( $0.56$  pc). It has a somewhat asymmetric or irregular bow shock, with features located at  $(+15'', -4'')$  and  $(+33'', 2'')$  in Figure 20c. It is possible that there may actually be two separate flows in Figure 20c, since there seem to be two separate bow shocks, and possibly also two separate collimated jets. For example, the feature labeled “jet” in Figure 20c resembles a series of small shocks in a collimated outflow, but it is off axis compared to some of the other features.

The average jet axis is roughly along  $P.A. \approx 106^\circ$ , and protrudes nearly perpendicular to the main ionization front,

aimed eastward into the interior cavity of NGC 3324. The driving source is not seen. There is some irregular structure west of the ionization front, including a cometary structure that may represent the position where the jet first breaks out of the dark cloud. If so, one would suspect the IR driving source to be located at roughly  $(-16'', +5'')$  in Figure 20c, or  $\alpha_{2000} = 10:36:54.0$ ,  $\delta_{2000} = -58:37:19$ . There is a red 2MASS source at this position, but deeper IR images with better angular resolution are needed for a confident comparison with the *HST* data. No clear shock structures are seen outside the region included in Figure 20c, nor is there a likely counter-jet visible in these images.

### 3.3.2 HH 1003

Figure 20d shows the region containing HH 1003. The most prominent structure in this outflow is a large ( $\sim 10''$ ) and well-defined bow shock that we denote as HH 1003C in Figure 20d. It shows a clear parabolic structure common to the main shocks in well-studied HH jets like HH 34, including detailed morphology consistent with a Mach disk near its apex. The main body of the jet that powers this bow shock is less clearly defined. Projecting back (north) along a line that bisects the bow shock, one sees structures consistent with a dense collimated jet body and collimated filaments that we denote HH 1003A in Figure 20d. Bright structures at the base connect back to the ionization front, perhaps marking the position where this flow breaks out of the molecular cloud. If this is the base of the jet, then the axis that connects it to the center of the bow shock runs along  $P.A. \approx 171^\circ$ . The group of filaments marked as HH 1003B may be part of the same flow (perhaps density enhancements at the sides of the outflow), a separate outflow, or unrelated filaments in the  $H\ II$  region that happen to lie near the axis of HH 1003.

We also draw attention to an interesting feature in the upper right corner of Figure 20d. In ground-based images with good seeing this structure resembles other proplyd candidates with a star at its apex, but its morphology in the *HST* images is not consistent with other proplyds. Instead, it may be a compact young  $H\ II$  region or wind-blown cavity around the star at its eastern edge. This star is located at  $\alpha_{2000} = 10:36:49.00$ ,  $\delta_{2000} = -58:38:04.9$ . The surrounding diffuse emission has strong  $H\alpha$  emission compared to  $[S\ II]$  and  $[O\ II]$ , suggesting photoionization by a relatively soft UV field – perhaps an early/mid B star. It would be interesting to obtain a classification spectrum of the central star, as it may represent a stellar wind bubble around a relatively isolated young B star still within its natal cloud.

### 3.3.3 HHc-1 in NGC 3324

The structure shown in Figure 20b resembles the main jet bodies of some other irradiated outflows that break out of edge-on ionization fronts. However, it appears to be less well-collimated than other features associated with jet bodies, and it lacks any clear evidence for a bow shock downstream. Its color indicates a strong  $[S\ II]/H\alpha$  ratio similar to other dense jets, but one cannot be confident that this is an outflow from a young star. Complex structures in dense photo-evaporative flows at ionization fronts can sometimes create features like this. Note, for example, the striated features

<sup>4</sup> The process by which these images were combined is described on the Hubble Heritage website: <http://heritage.stsci.edu/2008/34/index.html>.



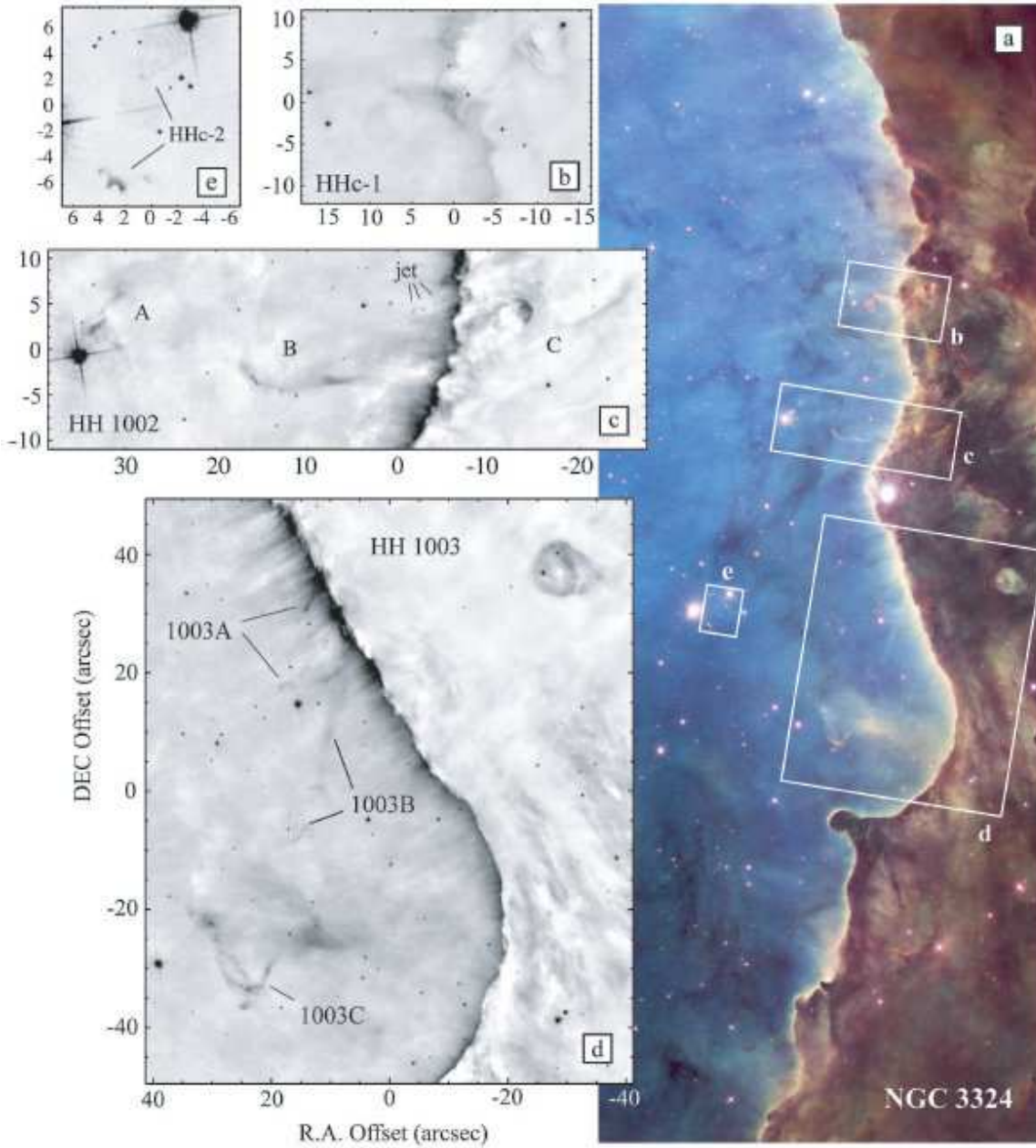


**Figure 20.** Outflows in the neighboring H II region NGC 3324. (a) The color image is a *Hubble Heritage* image composed of one ACS H $\alpha$  footprint (green), plus the same area covered with additional pointings using the WFPC2 camera in the [O III]  $\lambda 5007$  F502N filter (blue) and [S II]  $\lambda\lambda 6717, 6731$  F673N (red). The WFPC2 images in these two additional filters were obtained by the *Hubble Heritage* team. (The axes of the color image are rotated slightly with respect to R.A. and DEC.) (b) HH candidate jet 1, a [S II]-bright feature that apparently protrudes from the ionization front. (c) HH 1002 protrudes eastward from the edge-on ionization front. (d) HH 1003 has several parts, not necessarily all part of a single flow. HH 1003A appears to be a collimated jet plus internal working surfaces. HH 1003B may be side walls of the outflow or a separate flow. HH 1003C is a clear bow-shock plus Mach disk feature. The structure surrounding the star in the upper right corner of panel (d) may be a compact H II region or wind-blown bubble from a young star behind the ionization front. The nebular filaments in (e) may be shocks in an outflow, but no clear source or collimated jet can be identified so they are designated as part of a candidate outflow HHc-2. It is not clear if they are associated with any other jets in the image.

along the ionization front in Figure 20d. Therefore, we classify it as a jet candidate in Table 3, worthy of followup spectroscopy to study its kinematics or IR observations to search for an embedded IR source.

### 3.3.4 HHc-2 in NGC 3324

The nebular structures shown in Figure 20e constitute HHc-2 in NGC 3324. In the lower left of this panel is a connected group of condensations that may be knots within a flow. In the upper right of Figure 20e is a much fainter structure that is almost lost in the diffraction pattern of a bright neighbor-

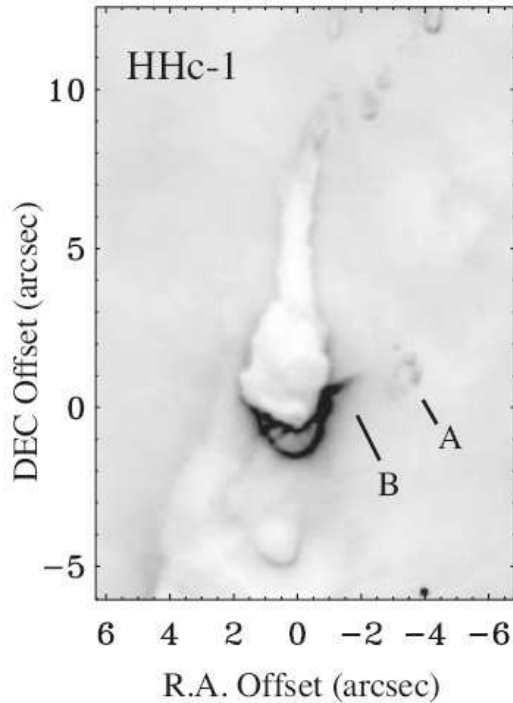


**Figure 21.** Candidate jet HHc-1 in Carina (this object is different from HHc-1 in NGC 3324). It is near HH 901 and 902, and can also be seen in Figure 5. The candidate jet extends to the west from a cometary globule that points toward Tr 14. Feature A may be a bow shock or working surface, whereas feature B appears to be the main body of the jet. Possible collimated features appear on the other side of the globule as well.

ing star, and its structure resembles a bow shock with the opening of the parabola pointed at P.A.  $\approx 320^\circ$ . If this represents a jet axis it points back roughly toward HH 1002 or HHc-1, although one cannot unambiguously associate it with either of those jets. The color of HHc-2 in the 3-color image is similar to the other HH jets and candidates in the same image, suggesting that these are photoionized nebular structures, possibly in a jet. Kinematics are needed before further conclusions can be drawn, however.

### 3.4 Comments on Individual Jet Candidates

As noted earlier, we identify over a dozen candidate jets that for one reason or another lacked structures that were clear enough to identify them as young star outflows based on morphology in images alone. We list these candidates in Table 3 as they provide good targets for followup spectroscopy to confirm or refute their nature as true jets. HHc-1 and HHc-2 in NGC 3324 were already discussed in the previous section; HHc-1 in Carina is discussed next.

#### 3.4.1 HHc-1 in Carina

Carina HHc-1 is shown in Figure 21, which is a detail of the larger field around HH 901 and HH 902 seen in Figure 5. The evidence for a jet in this image includes a possible collimated jet body emerging westward from the cometary cloud (feature B in Figure 21), and structures that resemble a small

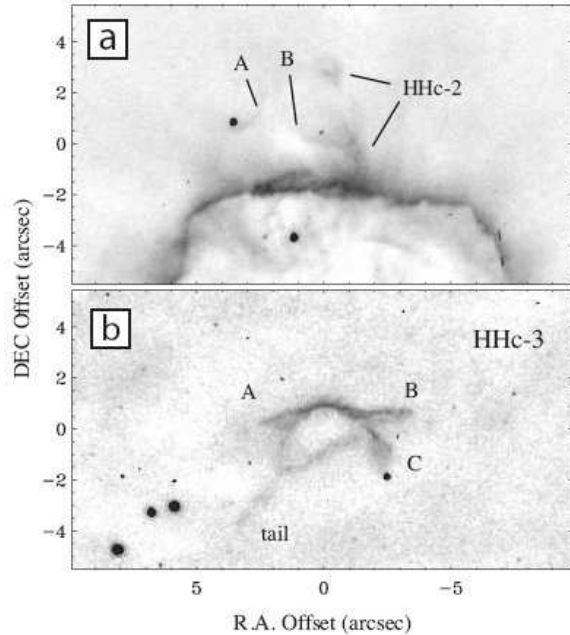


**Figure 22.** (a) Candidate jet HHc-2 in the South Pillars of Carina. This is a detail of the larger image seen in Figure 10. The possible jet HHc-2 is marked, emerging northward out of the pillar head. Two other features identified as wind bow shocks, identified as A and B, are discussed in the text. (b) Candidate jet HHc-3, with three possible collimated jets labeled A, B, and C emerging from a small cometary cloud. This image is just off the lower right of Figure 23.

bow shock or working surface in the jet (feature A). The position angle of this western portion of the jet is  $\sim 300^\circ$ , and the jet is  $\sim 4''$  (0.05 pc) long. There are also two spikes of emission on the east side of the cometary cloud, either of which may be a counter-jet in a bipolar flow.

Interestingly, there is a very faint point source along the putative jet axis, within  $0''.2$  of the tip of the cometary cloud, located at position  $(0'', 0'')$  in Figure 21. If HHc-1 is a true jet, then the driving source is likely to be this star embedded within the small cometary cloud. This is significant because, like HH 900, this dark cloud was one of the original proplyd candidates in Smith et al. (2003). While the object does not appear to be a photoevaporating disk like the proplyds in Orion, the jet candidate HHc-1 suggests that it does, in fact, contain an embedded protostar that is still actively accreting and driving an outflow. This adds further evidence that the large number of tiny cometary clouds suspended within the H II region cavity in Carina, as well as those in other regions like the similar cometary clouds in NGC 3603 (Brandner et al. 2000), are important potential sites of ongoing star formation.

#### 3.4.2 HHc-2

HHc-2 is shown in Figure 22a; again, note that this object is different from HHc-2 in NGC 3324. It is a concentration of nebulosity elongated northward from the head of a long and twisted pillar/cometary cloud in the South Pillars of Carina. This is the same pillar head which we suspect may contain the driving source of HH 1008 (the larger structure is shown

in Figure 10), which is a large bow shock located  $\sim 105''$  to the south. Emerging from the same pillar head in the opposite direction, HHc-2 may therefore be the counterflow to HH 1008, although this is quite speculative because the morphology of HHc-2 is not clearly that of a jet.

Interestingly, Figure 22a also shows two clear parabolic shock structures, each surrounding a star (objects A and B in Figure 22a). Their morphology and direction suggests that they are not jet bow shocks, but rather, stand-off shocks marking the collision between the winds of their stars and the photoevaporative flow off the nearby pillar head. Other examples of such structures are seen in our data, but they are not the main topic here.

### 3.4.3 HHc-3

HHc-3 in Figure 22b has an unusual appearance. One can clearly see a cometary cloud with a long and faint tail pointing southeast. There are three protrusions from the head of this cometary cloud, marked A, B, and C, which are candidate jets. Were it not for the fact that there are *three* protrusions, one might naturally claim that A and B (or alternatively, A and C) constitute a bipolar jet from a star within the cometary cloud, much like the more spectacular example of HH 900. If A and B are a bipolar jet, then the jet is fairly straight running east/west, but if A and C are a pair, then the jet is severely bent backward in a direction consistent with being bent by the same mechanism that shapes the cometary cloud and its tail. Either option seems plausible, as does the possibility that there are two separate flows. Spectra are needed to trace the kinematics of these features. (N.B.: HHc-3 is located very close on the sky to HHc-4, 5, 6, 7, and 8 discussed in the next section. It is just off the lower right corner of the main image in Figure 23.)

### 3.4.4 HHc-4, 5, 6, 7, and 8

In ground-based images, the elongated silhouette globule shown in the main frame of Figure 23 is a relatively inconspicuous dark clump. The high angular resolution afforded by *HST*, however, reveals evidence for bustling outflow activity from young stars embedded in it and immediately around it. Altogether, this activity suggests that this complex of silhouette globules likely represents the last vestiges of the dense cloud core at the head of a large dust pillar akin to others seen in the South Pillars or the Eagle Nebula (Hester et al. 1996) — although in this case, most of the surrounding dust pillar has already been photoevaporated away leaving only the densest parts as a cometary cloud complex amid newly exposed young stars. While there are many indications of likely outflow activity here, for each individual flow we prefer to await spectroscopic confirmation of their jet nature before assigning HH numbers, so we include likely outflows as candidate jets in Table 3.

HHc-4 in Figure 23d resembles the bow shocks seen in many well-studied HH jets. The parabola of the putative bow shock opens to the north, but in that direction the *HST* images show no clear evidence for other emission nebulosity associated with the body of the jet, and the driving source of the outflow is not clear. One might suspect its driving source to be an exposed young star about  $10\text{--}20''$  west of the head of the complex of dark clouds.

HHc-5 in Figure 23a is a collimated chain of clumps about  $4''$  ( $0.05$  pc) in length, stretched along P.A.  $\simeq 298^\circ$ . Similar to HH 1015, it seems to emerge from the northernmost tip of the complex of dark clouds in Figure 23. No clear bow-shock is seen at larger distances along the same axis.

HHc-6 in Figure 23b may be a bipolar jet much like HH 902 or HH 1010, bursting out from either side of the curved surface of the head of a pillar or cometary cloud. The putative jet has a total length of about  $18''$  ( $0.2$  pc). It runs nearly parallel to the curved limb-brightened edge of the cometary cloud, and because of this, it is difficult to be certain that it is in fact a jet and not a sharp edge-on ionization front. The putative jet axis is bent back toward the cloud, reminiscent of the many bent jets in Orion (Bally et al. 2006), so the P.A. listed in Table 3 is very rough. The case that this is in fact a jet would be strengthened if a luminous embedded IR source were detected near the edge of the ionization front along the jet axis near position  $(0'', 0'')$  in Figure 23b.

HHc-7 in Figure 23c is a relatively isolated bow-shock structure similar to HHc-4, with the opening of the parabolic shock structure pointing to the north. However, in this case there is some intriguing (although unclear) evidence of a possible jet and source. Looking  $30\text{--}40''$  to the northeast, one sees a faint chain of aligned filaments that may lead back to a star within a curved ionization structure that resembles some of the large proplyds in Orion — especially HH 668 and its source (Smith et al. 2005b). This possible source of the HHc-7 jet is located at offset position  $(+7'', +48'')$  in the main panel of Figure 23.

Lastly, HHc-8 shown in Figure 23c is an LL Ori-like object. No clear jet structure is seen, but the class of LL Ori objects have been linked to jet outflows that are bent by a side wind, radiation pressure, or the rocket effect (Bally et al. 2006). This cometary-shaped nebular structure implicates a radiation or wind source located to the west, and it has a bright star at its apex.

### 3.4.5 HHc-9

HHc-9 shown in Figure 24 is a large and smoothly curved bow shock structure. There is tenuous evidence for a Mach disk at its apex, implying that the jet direction is due west. This would also imply that any hypothetical collimated jet and driving source, not detected here, would be off the left edge of the field, since HHc-9 fell near the edge of the detector at the boundary of the large mosaic including Tr 14. HHc-9 could also plausibly be a density enhancement in a stellar wind bubble that is illuminated by Tr 14.

### 3.4.6 HHc-10

HHc-10 is shown in Figure 25. It is a series of curved shock structures associated with the head of a very large dust pillar that also contains the driving source of HH 903, located about  $90''$  south. An image of the larger field including HH 903 is shown in Figure 6. The head of this pillar appears to have active star formation, including an embedded cluster that is just beginning to emerge. There is likely to be outflow activity associated with these sources. If HHc-10 is a group of outflows of this type, the flows appear to be deflected toward the south by radiation pressure or a large-scale flow in

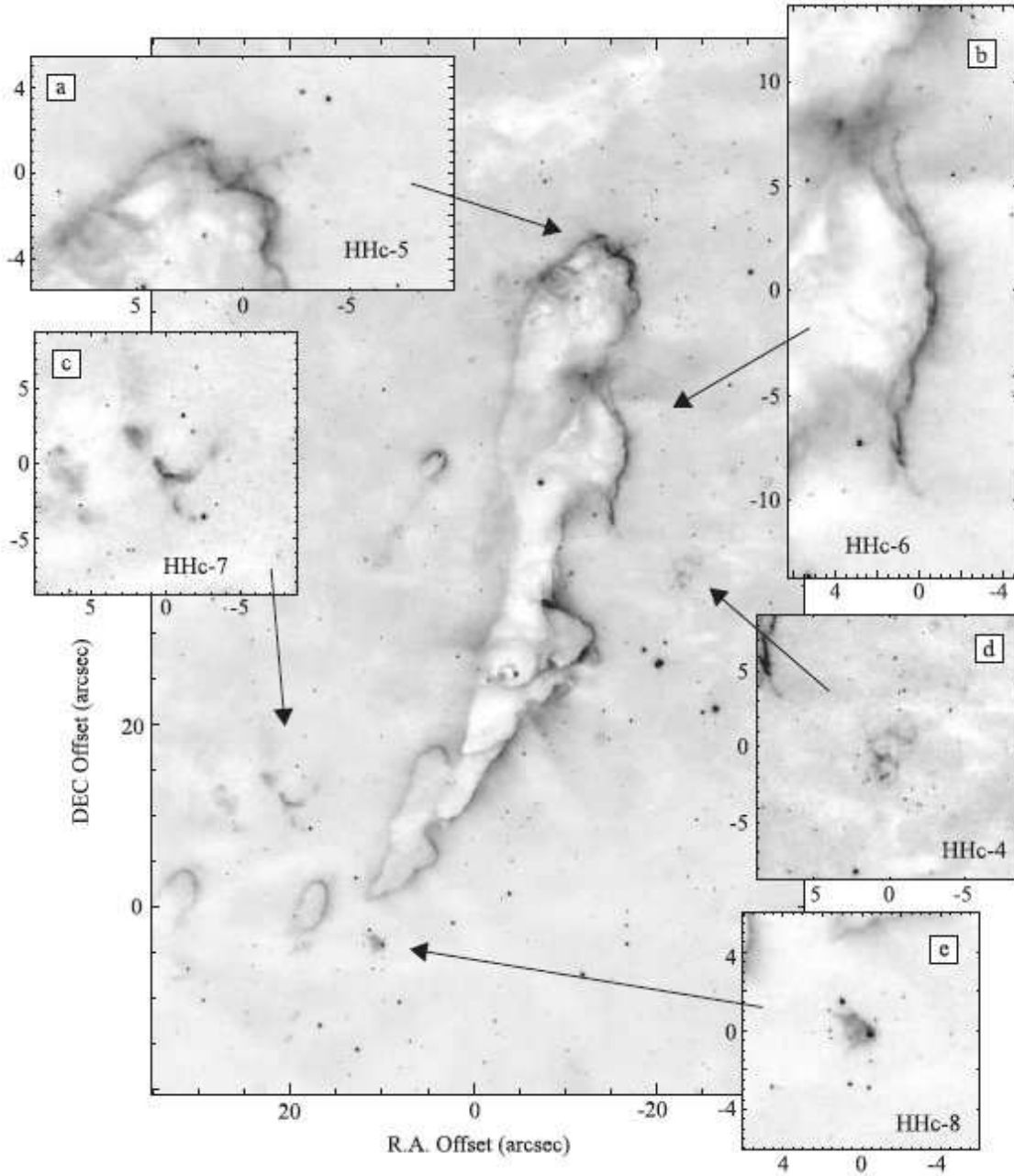


**Figure 23.** Several HH jet candidates associated with a complex of dense molecular globules in the South Pillars. (a) Carina HHc-5 appears to be a collimated chain of ionized knots protruding from the head of the globule. No counter-jet is seen. (b) HHc-6 may be a bipolar jet flowing north and south from a clump on the west edge of the globule. The candidate jet flows nearly parallel to the edge-on ionization front and appears to be swept back (curved) toward the globule. (c) HHc-7 is a bow shock with an unclear origin. It may be associated with the proplyd-like object located  $30''$  north-west. (d) HHc-4 is also a bow-shock structure with an unclear origin. (e) HHc-8 is an LL-Ori or proplyd-like object with cometary shape surrounding a bright central star.

the H II region ( $\eta$  Car and Tr 16 are located to the north). However, because of this complexity and because of the lack of a clear collimated jet body, these features could also be photoevaporative flows off the surface of the pillar head that are deflected and shaped by the same mechanism. Therefore, HHc-10 is a candidate outflow in Table 3.

#### 3.4.7 HHc-11

HHc-11, shown in Figure 26, is another case of an orphan bow shock structure without clear evidence for a collimated jet and no good candidate for a driving source. It is located several arcminutes south of HH 1006. While its location may be consistent with being part of that flow if the flow has some bend in its axis, the line of symmetry through the arc in HHc-11 does not point back toward HH 1006, so an association with this jet seems unlikely.

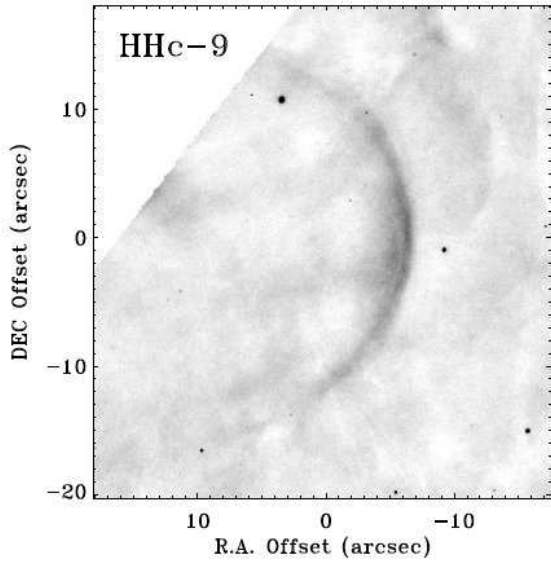


**Figure 24.** Candidate jet bow shock HHc-9 located near the Tr 14 cluster, which is off the far right of the image. This object fell near the edge of the large Tr 14 mosaic; no body of the jet or driving source can be seen; they would be off the image.

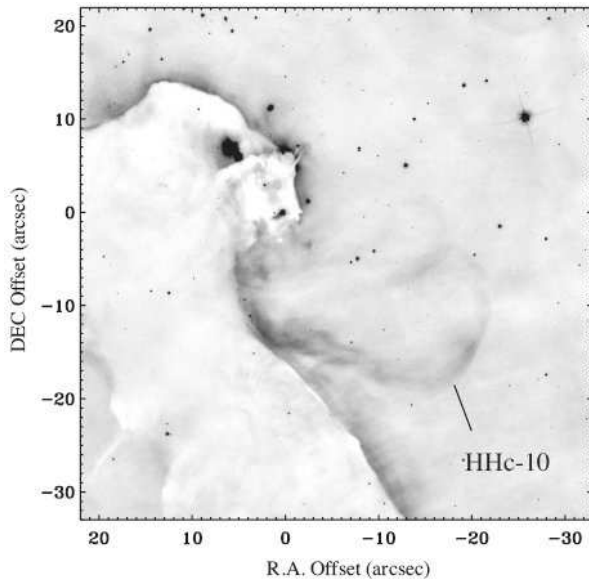


**Figure 25.** Candidate outflow HHc-10, associated with the head of one of the most prominent dust pillars in Carina. This is a detail of the field north of HH 903 (see Figure 6).

#### 3.4.8 HHc-12

Another orphan shock structure, HHc-12 in Figure 27, shows two curved shocks plus a collection of fainter emission knots. The curved shocks are reminiscent of two overlapping bow shocks, but the identification of this as part of a true protostellar outflow is uncertain. It is not obviously associated with any collimated jet, and the morphology of its nebular emission is not obviously that of a parabolic bow shock. It is however, very near on the sky to HHc-3 (about  $30''$  to the upper right on Fig. 27) and also close to the complex of

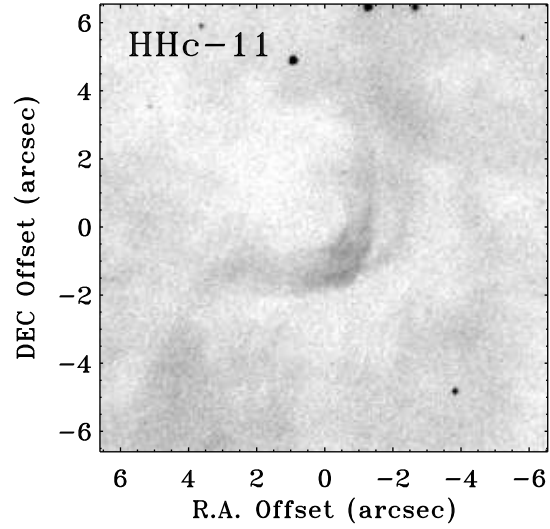


**Figure 26.** Candidate jet bow shock HHc-11 amid the South Pillars in Carina. No collimated jet or driving source is seen.

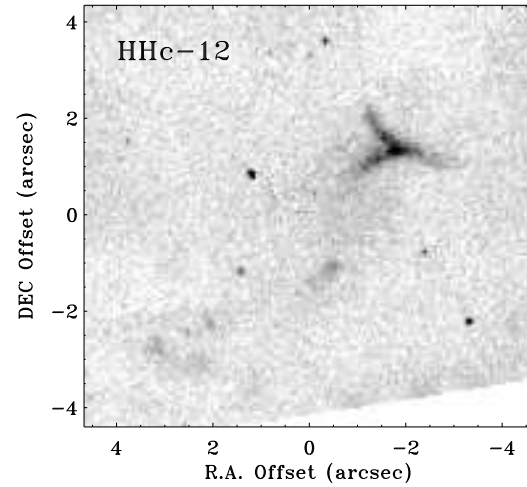


**Figure 27.** Candidate shock structure HHc-12 amid the South Pillars in Carina. No collimated jet or driving source is seen, although this structures are located about  $30''$  southeast of HHc-3. It is also located just off the bottom of the image in Figure 23, containing the complex of globules housing jet candidates HHc-4, 5, 6, 7, and 8.

molecular globules and jet candidates in Figure 23. HHc-12 may be a distant shock in one of these jets.

#### 3.4.9 HHc-13

HHc-13, shown in Figure 28, is a candidate microjet flowing at  $P.A. \simeq 165^\circ$  from a moderately bright star located about  $1'$  NE of the dust pillar from which HH 666 emerges (see Fig. 3). It appears to be highly collimated, with an unresolved width, and a length that can be traced to  $\sim 2''$  ( $0''.22$  pc) from the star where its surface brightness falls below the detection limit. The P.A. of this elongated radial feature is different from the diffraction spikes in the PSF of the image,

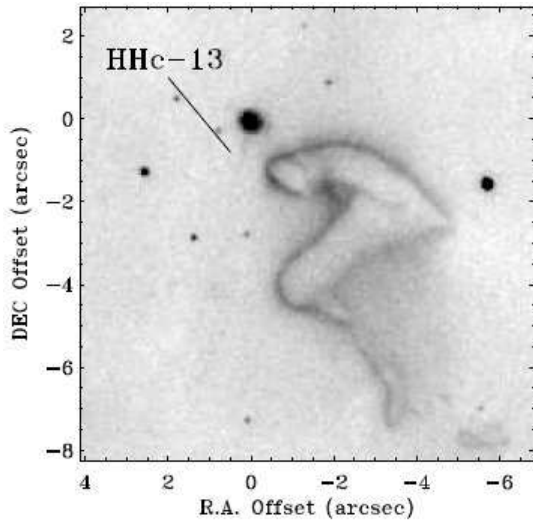


**Figure 28.** Candidate microjet HHc-13, from a star located about  $1'$  NE of the origin of HH 666 (see Figure 3).

which can also be seen in some brighter stars in Figure 3 to be at roughly  $110^\circ$  and  $200^\circ$ , so it is a real nebular feature. Without kinematic information it is difficult to be sure that it is a true jet, however.

#### 3.4.10 HHc-14

The candidate jet shocks comprising HHc-14 are near HH 1014 and can be seen in Figure 16. Their curved structure may denote partial illumination of a bow shock structure, but this is unclear. Given the direction at which the HH 1014 jet emerges from its dust pillar, it seems unlikely that HHc-14 is part of the same flow. It may come from an IR source embedded in a different pillar head.

#### 3.4.11 HHc-15 and Proplyds in the Core of Tr 14

Figure 29 shows a detail of the *HST*/ACS F658N image in the core of the Tr 14 cluster, revealing the discovery of several extended objects seen on small scales. HHc-15 is a candidate microjet, made of a collimated chain of emission clumps stretching about  $2''$  ( $0.02$  pc) eastward at P.A.  $\simeq 85^\circ$  from a visible star. Without kinematic information or spectra of the stars in this field, however, one cannot be certain that it is a jet or which star is its driving source.

Immediately east of HHc-15 is a thin circumstellar nebula 104354.91-593245 (following the coordinate-based naming convention of Smith et al. 2003). It is shown in the detail panel in the upper right of Figure 29. This object has a limb-brightened shell-like appearance, and may be a circumstellar shell, wind bow shock, or a proplyd envelope. It has a radius of 2000–3000 AU, comparable to some of the larger proplyds in Orion (for background on Orion’s proplyds, see O’Dell 2001; Bally et al. 2000; Smith et al. 2005b). In the lower-middle portion of Figure 29, there is a star surrounded by a very irregular shell structure 104355.49-593255, also shown in a detail panel second from right at the top of Figure 29. This object has rather chaotic structure; perhaps it is a shell

or proplyd envelope like 104354.91-593245, but which is being disrupted by stellar winds from multiple nearby O-type stars in the cluster.

In the upper left of Figure 29, one sees two extended nebular objects around stars that are good candidates for proplyds in Tr14, 104356.58-593244 and 104356.62-593246. (These are also shown in the second-from-left panel at the top of Figure 29.) The larger object in particular, 104356.58-593244, has a long  $\sim 3''$  tail running away from the O2-type supergiant HD 93129A (see Walborn et al. 2002), and is almost certainly a proplyd. Lastly, a bright source 104357.03-593251 is located very close to HD 93129A in the western part of its diffraction pattern. As shown in the detail panel in the upper left corner of Figure 29, however, this object is not a point source. It has extended H $\alpha$  emission within a radius of  $0''.5$  (1,000 AU), and is probably a marginally resolved evaporating protoplanetary disk.

The detection of probable microjets and proplyds in the core of Tr 14 is an interesting and surprising discovery in these new F658N narrowband *HST*/ACS images. These structures were not seen in *HST*/ACS images with the High Resolution Channel (HRC) by Maíz Appelániz et al. (2005), presumably because they were too faint in the broadband F435W (*B*-band) and F850LP filters. This suggests that the extended emission in Figure 29 is H $\alpha$  line emission and not starlight scattered by circumstellar dust. Jets and proplyds associated with stars in the core of Tr 14 would require that some of these stars have retained their protostellar disks, despite their violent neighborhood in the core of Tr 14 — this location is far more extreme than the Trapezium, with the O2 supergiant HD 93129A and several other early O-type stars within only 0.1–0.2 pc. This is even more surprising when one considers that Tr 14 is also older than the Trapezium, with an age of 1–2 Myr (see Walborn 2009; Smith 2006a; and references therein). These structures in Tr 14 therefore warrant intensive followup study, since they provide information about the survival of resilient protoplanetary disks in harsher environments and over a longer time than in the very young Trapezium (age  $\sim 10^5$  yr). Spectra of the central stars associated with these extended features in Tr 14 would be valuable, and high-spatial-resolution thermal-IR observations are encouraged to determine if these features resemble the mid-IR emission from proplyds in the Trapezium (e.g., Smith et al. 2005d).

## 4 A CLOSER LOOK AT HH 900, 901, AND 902

Figures 30 and 31 show intensity tracings ( $I_{H\alpha} = 10^{-15}$  ergs  $s^{-1} cm^{-2} arcsec^{-2}$ ) along the jet axes of HH 900, HH 901, and HH 902. These are intensities averaged over a few pixels, with extraction widths corresponding roughly to the widths of the jet bodies. (These intensities are measured from the specific intensity in our F658N ACS images using the pipeline calibration, integrated over the width of the F658N filter.) In the images, all three jets show a qualitatively similar structure, with the inner parts showing a well-collimated bipolar jet body, and with bow shocks at their outer extremities. This structure is clearly defined in HH 900 and HH 901, and somewhat less so in HH 902 where the jet skirts along the ionization front at the edge of its par-



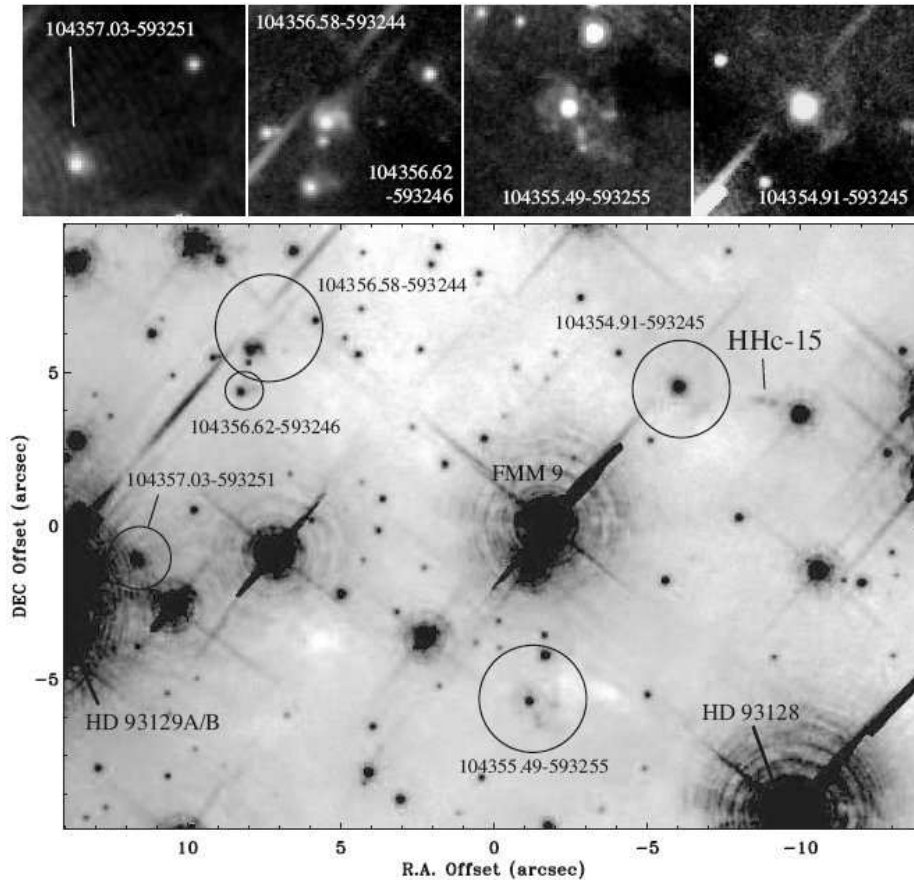


**Figure 29.** The core of the Tr 14 cluster in an H $\alpha$  ACS/WFC image. The candidate microjet HHc-15 is in the upper right, and several other extended objects that are possible proplyds are circled. Postage stamps of these individual extended objects with a different intensity scale are shown in the four panels at the top. The brightest cluster members with HD designations are noted, as well as star 9 from Feinstein, Marraco, & Muzzio (1973) in the center of the image.

ent dust pillar and where there are multiple overlapping bow shocks instead of two large opposing shocks. The implication is that in the inner parts of the jet, within a few arcseconds of the embedded driving source, the jet body is still well defined because it has flowed relatively unimpeded. As time continues and the jet material moves farther from its point of origin, differences in velocity along the flow can become more important. Faster material overtakes older slower material at internal shock surfaces, forming dense clumps, so that the jet eventually takes on the structure of a series of bullets rather than a smoother continuous stream. Bullets or knots may also arise from an intermittent jet source, of course.

In the intensity plots, this progressive clumping of the jet is manifested as spatially continuous emission within a few arcseconds of the jet origin, followed by much larger variations in the intensity on/off individual knots at larger separations. (The intensity tracings for HH 902 are complicated because some of this apparent continuous emission at offsets of  $-2''$  to  $-7''$  arises from emission at the ionization front. The jet body at positive offsets along the jet axis in Figure 31 is less contaminated.) At increasing separation and increasing clumpiness, the H $\alpha$  intensity does not drop as  $r^{-2}$  as one might expect from a conical jet. Although the density drops in the regions between clumps, the emission

measure is dominated by material that is piling-up at internal shocks where the density may be increasing. Strong peaks in the H $\alpha$  intensity occur at the terminal bow shocks along the flow, signifying a strong pile-up of jet material there. Note that in cases where the jet body has a substantial neutral H fraction, one expects roughly constant  $I_{H\alpha}$  since the gas is ionization bounded (e.g., Bally et al. 2006).

All three jets show some deviation from a perfectly straight flow along a single axis, and in three different ways. As noted earlier, in HH 900 the jet appears to be bent *toward* the direction of the dominant radiation and stellar wind sources in Tr 16. For this source, we concentrate on the western part of the flow in Figure 30. In contrast, the HH 901 jet is clearly bent *away* from the massive cluster of O-type stars in Tr 14, with a difference of  $\sim 7^\circ$  between the axes of its two opposing flows. It is not immediately clear, however, if this is really a bend in the flow axis or a non-uniform irradiation effect (see below). Finally, for HH 902 in Figure 31, parts of the jet body deviate from the jet axis as they seem blown back, away from the hot O stars, whereas the densest knots seem to remain right along a single straight jet axis. If some of the jet material is getting blown away while dense knots remain, this introduces potential pitfalls in trying to deduce jet properties like the mass-loss rate from distant knots in a flow. In the following section, therefore, we estimate mass-

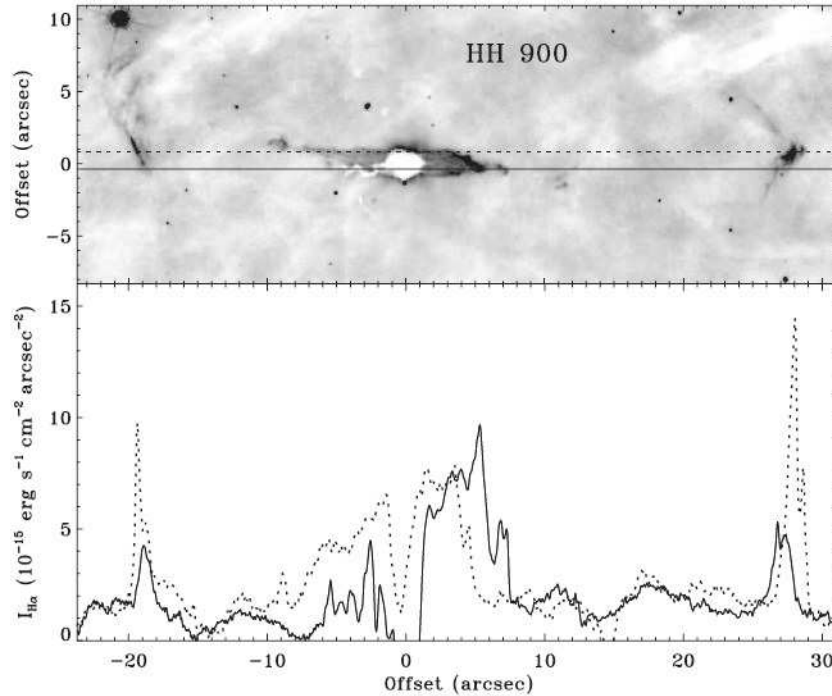


**Figure 30.** A rotated image of HH 900 (top) and two intensity tracings along different samples of the jet (bottom). The solid and dotted tracing correspond to the respective lines in the top panel. The widths over which we sample the average intensity was 4 pixels, or  $0''.22$ . The observed intensity,  $I_{H\alpha}$ , is plotted in units of  $10^{-15} \text{ erg s}^{-1} \text{ cm}^{-2} \text{ arcsec}^{-2}$ , and neglects possible contributions from [N II].

loss rates from the inner and fairly continuous collimated parts of the jets when possible.

The  $H\alpha$  intensity can be used as a direct tracer of the electron density if the size of the emitting jet body is resolved so that one can infer an emitting path length. Assuming a fully ionized jet and assuming that [N II]  $\lambda 6583$  makes a relatively unimportant contribution to the emission detected in the F658 filter for these jets, one can then take the  $H\alpha$  intensity to infer the true density in the jet. This is important for our estimates of  $\dot{M}$  for Carina's HH jets, as described in the following section. In irradiated jets, [N II]  $\lambda 6583$  makes a small contribution to the emission in the filter, so neglecting it introduces a small uncertainty compared to other sources of uncertainty. A more serious source of error may be the assumption that the jet material is fully ionized. In several irradiated HH jets in Orion, for example, Bally et al. (2006) suspected significant neutral H fractions in the jets, in some cases leading to jet bending through the rocket effect when a photoionizing source is located to one side. HH 901 may be a good example of this phenomenon. Close examination of the inner jet structure shows a thin bright edge on the side of the jet body that faces Tr14 (down in Figure 31), whereas the other (north) side of the jet body has lower surface brightness and is more diffuse. This points to a lower electron density there, possibly due to a lower ionization fraction if this side of the jet is shielded from the UV radiation by the neutral jet core. The bend direction of the jet axis is in accord with this hypothesis. If there is a substantial neutral fraction in the jets that are so close to a strong UV source like Tr 14, then the densities and mass-loss rates for all jets discussed below should be taken as lower limits.

## 5 JET MASS-LOSS RATES

To estimate the mass-loss rates of the new HH jets in Carina, we first estimate electron densities from the intensity measured in images. The  $H\alpha$  emission measure in an ionized nebula depends on the electron density,  $n_e$  as well as the emitting path length  $L$  through the object. For a collimated jet, we take  $L$  to be the diameter of the jet body, or  $R = L/2$ . Table 4 lists estimates for  $L$  for each HH jet and jet candidate taken from spatially resolved jet structures in our ACS images. An expression between  $n_e$ ,  $L$ , and the emission measure can be simplified to

$$n_e = 15.0 \sqrt{\frac{I_{H\alpha}}{L_{pc}}} \text{ cm}^{-3} \quad (1)$$

where  $I_{H\alpha}$  is the  $H\alpha$  intensity measured in our narrowband F658N ACS images in units of  $10^{-15} \text{ erg s}^{-1} \text{ cm}^{-2} \text{ arcsec}^{-2}$ , and  $L_{pc}$  is the emitting path length through the jet in pc (see Smith et al. 2004c; Bally et al. 2006; Walawender et al. 2004). Table 4 lists measured values of  $I_{H\alpha}$  and the corresponding estimates of  $n_e$  calculated in this way. Obviously there is wide variation in both  $I_{H\alpha}$  and  $n_e$  at different positions in each jet. The values of  $I_{H\alpha}$  are therefore typical average values of bright emission features in the jet flow taken to be representative of the inner jet. We account for variations in  $I_{H\alpha}$  along the jet (sharp drops in intensity in Figure 31, for example) with a geometric filling factor  $f$ , as noted below, since the observed density that causes the observed emission measure does not uniformly fill the column of the jet.

To provide rough estimates of the mass-loss rates for the Carina HH jets from the electron densities in Table 4,

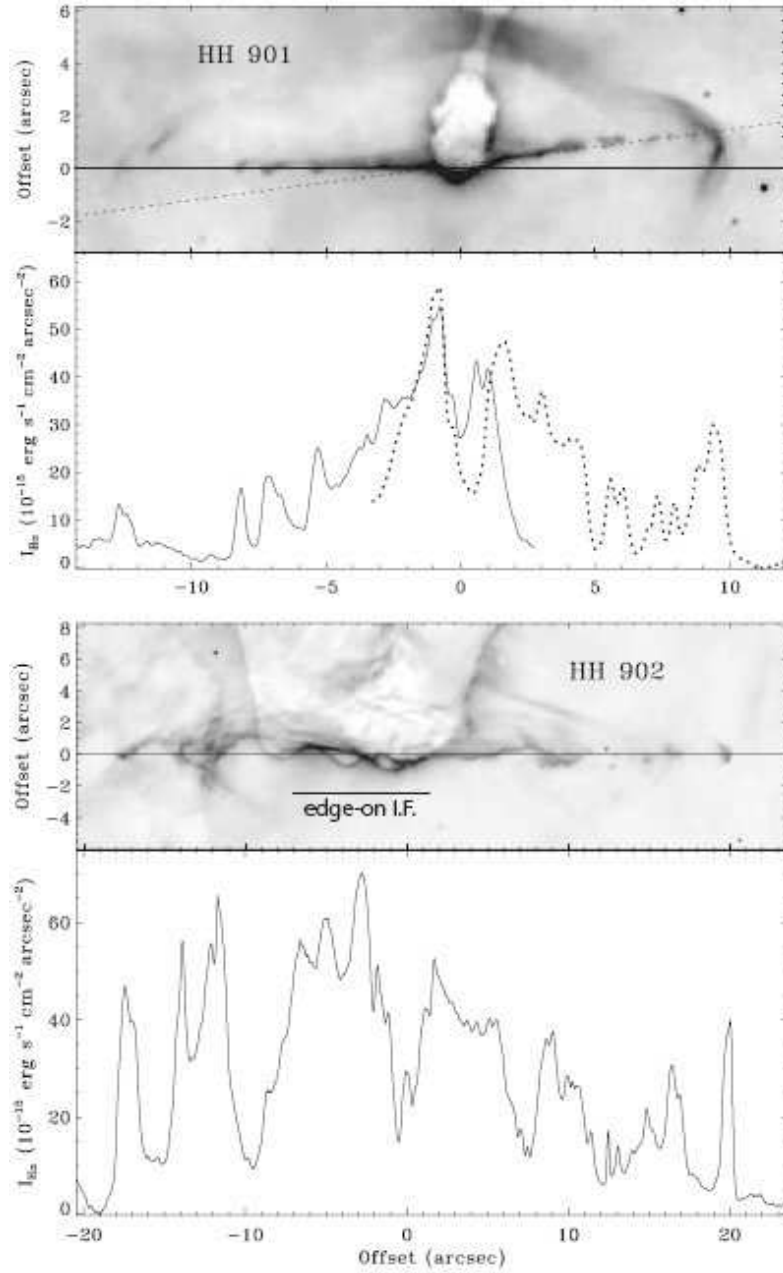


**Figure 31.** Same as Figure 30, but for HH 901 and HH 902. For HH 901, we show tracings along two separate directions in order to follow the bend in the jet. The solid and dashed tracings correspond to the left and right sides of the jet, respectively.

we treat the jets as approximately cylindrical. Therefore, the portions of the jets where we have chosen to measure representative values of  $L$ ,  $I_{H\alpha}$ , and  $f$  correspond to inner parts of the jet that are well collimated, such as HH 666 M and the inner parts of HH 900, 901, and 902 discussed in the previous section. Even so, clumping at internal shocks begins to affect the emissivity, so to account for this effect (bright knots separated by empty relatively spaces) we adopt a geometric filling factor  $f$ , estimated from the morphology in images. Note that for HH 666 M, where we measure  $\dot{M}$  separately for a bright knot and a fainter region between knots, the derived mass-loss rate differs by only  $\sim 20\%$ . For HH objects like HH 1003C, 1008, 1009, HHc-4, etc., where

clear bow shocks but no clear collimated jet can be seen, we cannot provide estimates of  $\dot{M}$  in this way, although we do give estimates of  $n_e$ . Adopting cylindrical structure for the collimated jets that we can measure, then, the average mass-loss rate flowing through *one side* of the jet is given by

$$\dot{M} = \mu m_H n_e V \pi (L/2)^2 f \quad (2)$$

where  $\mu=1.35$  is the mean molecular weight,  $m_H$  is the proton mass,  $V$  is the jet speed, and  $f$  is a geometric filling factor inferred from structure in images. To represent the total mass carried away by both sides of a bipolar jet, this number must be multiplied by 2. Numerically, this can then be expressed as

**Table 4.** Physical Paramters for HH Jets and jet candidates in Carina

HH	$L_{pc}$ (pc)	$I_{H\alpha}$ (erg/s cm <sup>-2</sup> arcsec <sup>-2</sup> )	$f$	$V_{200}^a$ (10 <sup>2</sup> km/s)	$n_e$ (cm <sup>-3</sup> )	$\dot{M}_{jet}$ (10 <sup>-9</sup> $M_{\odot}$ yr <sup>-1</sup> )	Comment
666 M	0.005	$11.0 \times 10^{-15}$	1.0	1.0	705	190	inner jet between clumps
666 M	0.005	$15.9 \times 10^{-15}$	1.0	1.0	847	274	bright knot
900	0.02	$6.1 \times 10^{-15}$	0.5	1.0	263	568	wide inner jet, east
900 microjet	0.0025	$9.3 \times 10^{-15}$	1.0	1.0	916	620	bipolar microjet from star
901 E	0.0035	$30 \times 10^{-15}$	1.0	1.0	1390	184	inner jet, east
901 W	0.0035	$14.0 \times 10^{-15}$	0.3	1.0	920	40	clumps, west
902 W	0.0031	$40 \times 10^{-15}$	1.0	1.0	1700	176	inner jet, west
903 jet	0.0047	$11.0 \times 10^{-15}$	1.0	1.0	730	172	inner jet body
1002	0.0034	$2.5 \times 10^{-15}$	...	...	400	...	no clear jet body
1003 A	0.004	$3.7 \times 10^{-15}$	0.5	1.0	455	38	inner jet body near I.F.
1004 NE	0.0067	$7.4 \times 10^{-15}$	0.5	1.0	497	120	inner jet body, unclear morph.
1005	0.0044	$11.0 \times 10^{-15}$	0.8	1.0	750	124	inner jet body
1006 N	0.0037	$2.5 \times 10^{-15}$	0.5	1.0	390	28	thin jet body, north
1006 S	0.0034	$2.4 \times 10^{-15}$	0.4	1.0	403	20	thin jet body, south
1007	0.0022	$4.4 \times 10^{-15}$	1.0	1.0	671	35	jet body
1008	0.0078	$9.8 \times 10^{-15}$	...	...	530	...	no clear jet body
1009	0.0028	$4.9 \times 10^{-15}$	...	...	630	...	no clear jet body
1010 SW	0.0073	$2.9 \times 10^{-15}$	0.4	1.0	299	68	inner jet body
1011	0.0028	$7.4 \times 10^{-15}$	0.8	1.0	769	52	microjet body
1012 microjet	0.0016	$2.5 \times 10^{-15}$	0.5	1.0	960	13	microjet body, not LL Ori shock
1013	0.0037	$8.6 \times 10^{-15}$	0.2	1.0	723	21	jet body NE, but unclear
1014	0.004	$7.1 \times 10^{-15}$	0.4	1.0	632	44	clumpy jet body
1015	0.0028	$0.74 \times 10^{-15}$	0.4	1.0	244	8.4	faint, thin jet body
1016	0.0019	$7.4 \times 10^{-15}$	1.0	1.0	934	36	bow shock, unclear jet body
1017 jet	0.0016	$4.4 \times 10^{-15}$	0.5	1.0	787	11	inner jet body
1018 microjet	0.0011	$6.4 \times 10^{-15}$	1.0	1.0	1140	15	microjet
HHc-1 (3324)	0.0056	$4.9 \times 10^{-15}$	0.5	1.0	444	76	unclear jet body
HHc-2 (3324)	0.0045	$8.6 \times 10^{-15}$	1.0	...	660	...	no clear jet body
HHc-1 B	0.0028	$35.6 \times 10^{-15}$	1.0	1.0	1690	144	microjet body, west
HHc-2	0.0022	$24.5 \times 10^{-15}$	0.4	1.0	1580	33	unclear jet body
HHc-3 ABC	0.0019	$3.7 \times 10^{-15}$	0.5	1.0	660	13	average of ABC components
HHc-4	0.0034	$6.4 \times 10^{-15}$	...	...	650	...	bow shock only, no clear jet body
HHc-5	0.0031	$2.2 \times 10^{-15}$	0.3	1.0	400	12	unclear jet body
HHc-6 N	0.0028	$4.4 \times 10^{-15}$	0.8	1.0	595	40	curved jet body, north
HHc-6 S	0.0028	$7.4 \times 10^{-15}$	0.8	1.0	769	52	curved jet body, south
HHc-7	0.0037	$9.8 \times 10^{-15}$	...	...	770	...	bow shock only, no clear jet body
HHc-8	0.0028	$6.1 \times 10^{-15}$	...	...	700	...	LL Ori shock, no clear jet
HHc-9	0.01	$4.2 \times 10^{-15}$	...	...	306	...	bow shock only, no clear jet body
HHc-10	0.0067	$6.1 \times 10^{-15}$	...	...	450	...	no clear jet body
HHc-11	0.0034	$3.7 \times 10^{-15}$	...	...	490	...	no clear jet body
HHc-12	0.0022	$3.7 \times 10^{-15}$	...	...	613	...	no clear jet body
HHc-13	0.0012	$2.9 \times 10^{-15}$	1.0	1.0	737	12	microjet
HHc-14	0.0028	$3.7 \times 10^{-15}$	...	...	544	...	no clear jet body
HHc-15	0.0012	$15.0 \times 10^{-15}$	0.5	1.0	1650	13	microjet

<sup>a</sup>Except for HH 666,  $V_{200}=1$  is an assumed value in lieu of measurements for the jet speeds.

$$\dot{M} = 1.1 \times 10^{-5} (n_e V_{200} L_{pc}^2 f) M_{\odot} \text{ yr}^{-1} \quad (3)$$

where  $V_{200}$  is the jet speed in units of 200 km s<sup>-1</sup>. This expression is used to calculate the values of  $\dot{M}$  in Table 4, which also lists adopted values of  $V_{200}$  and  $f$ . Using only a single-epoch of images and no kinematic information, we can make only rough estimates of the characteristic mass-loss rates for the Carina jets. Better estimates will come from future studies that can provide proper motions with multi-epoch images and Doppler shifts from high resolution spectra. For now, we adopt  $V_{200} = 1.0$  as a fiducial value for all. In HH 666, spectra show speeds of roughly 200 km s<sup>-1</sup> for HH 666 M and O (Smith et al. 2004c), and this is a typical speed for the inner parts of HH jets. Also, we will be comparing these jet mass-loss rates to those derived in the same way for jets in the Orion Nebula, for which Bally et al. (2006) adopted 200 km s<sup>-1</sup> for the speed of most jets.

There are, of course, considerable uncertainties in the estimates of  $\dot{M}$  in Table 4. As noted above, the denser jets have an unknown neutral H fraction, the filling factor  $f$  that we adopt is rather subjective, and the jet speed is not known for all sources except HH 666. Although the choice of fill-

ing factor is subjective, it is guided by the jet structure in high resolution images, and is likely to be reliable to within  $\pm 30\%$ . Judging from a wide array of observations of HH jets, the adopted velocity of 200 km s<sup>-1</sup> is a representative choice, introducing a factor of  $\sim 2$  uncertainty. Fortunately, more accurate estimates of the jet speed and possibly also the ionization fraction can be obtained with more detailed spectroscopic followup and a later epoch of *HST* imaging to measure proper motions of the jets (these observations are needed to confirm the candidate jet objects anyway). The estimates of  $\dot{M}$  are probably good to within a factor of 2–3 or perhaps somewhat more, and are adequate to convey the rough distribution of jet mass-loss rates that we are sensitive to. This level of accuracy is comparable to expected intrinsic variability of the mass-loss rate over time for an individual jet anyway. For the one case where detailed spectroscopic observations are available, HH666, it is reassuring that the electron density derived from the emission measure in image data (Table 4) agrees with the electron density derived from spectral diagnostics like the [S II] doublet intensity ratio (Smith et al. 2004c).

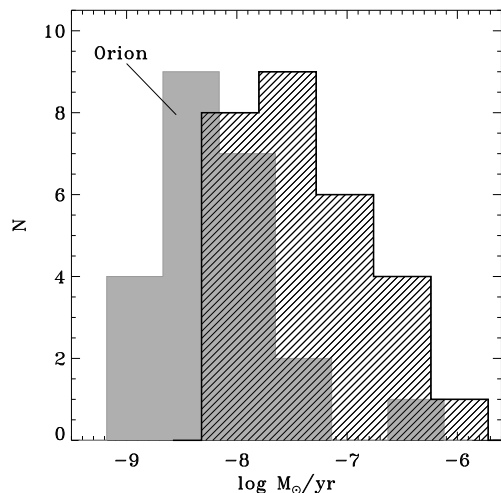


**Figure 32.** A histogram of the HH jet mass-loss rates from Table 4 (black with hatched pattern). For comparison, the filled gray histogram shows mass-loss rates for a sample of a comparable number of HH jets in the outer Orion Nebula, taking the value of  $\dot{M}_0$  listed in Table 6 of Bally et al. (2006), but multiplied by 2 to account for contributions from both sides of a bipolar jet, as we have done for Table 4 (see text). These Orion mass-loss rates were derived using the same method we adopted for Carina.

While the electron density is subject to uncertain estimates of  $L$ , we note that there is not much variation in derived values of  $n_e$  in Table 4, which vary by less than a factor of 10 (200 to 2000  $\text{cm}^{-3}$ ). In general, the fainter jets have  $n_e$  of a few  $10^2 \text{ cm}^{-3}$ , while the brightest jets have densities around or slightly above  $10^3 \text{ cm}^{-3}$ . The faint end is likely a selection effect, in the sense that lower  $\dot{M}$  jets with densities near or below  $10^2 \text{ cm}^{-3}$  would have emission measures fainter than fluctuations in the background H II region and would be difficult to detect. Jets with densities much above  $2000 \text{ cm}^{-3}$  might have dense jet cores that remain largely neutral, despite the strong UV radiation, so that H $\alpha$  emission does not necessarily trace the jet mass (e.g., Hartigan et al. 1994). This is another reason to suspect that for the densest jets, then, it is likely that the mass-loss rates and densities in Table 4 are underestimates.

We measure a range of mass-loss rates ranging from  $8 \times 10^{-9} M_\odot \text{ yr}^{-1}$  up to  $\sim 10^{-6} M_\odot \text{ yr}^{-1}$ . These jet mass-loss rates trace a range of active accretion rates onto their driving protostellar sources. If one assumes that the mass-loss rate of the jet is roughly 10% of the accretion rate onto the star (e.g., Calvet 1997), the observed jet mass-loss rates in Carina imply relatively high mass accretion rates of  $10^{-7}$  to  $10^{-5} M_\odot \text{ yr}^{-1}$ . (If the visible HH jet is only some fraction of the wind driven from the protostellar disk, then implied accretion rates are even higher.) These are on the high end for the distribution of mass accretion rates measured for nearby sources (e.g., Calvet et al. 2000), so the high mass-loss rate jets in our sample may trace more massive protostars or brief episodic accretion/outflow events akin to FU Ori outbursts. Indeed, mass accretion rates around  $10^{-5} M_\odot \text{ yr}^{-1}$  are comparable to the episodic bursts of accretion inferred to occur in early protostellar phases (Calvet et al. 2000). Jets in our sample with more typical mass-loss rates around  $10^{-7} M_\odot$

$\text{yr}^{-1}$  are comparable to those of famous nearby HH jets like HH 34, 47, and 111 (e.g., Hartigan et al. 1994).

Figure 32 illustrates a consequence of selection effects determining the lower jet densities that we are sensitive to. This is a histogram of the mass-loss rates for Carina HH jets in Table 4 (black hatched) compared to a similarly sized sample of HH jets in Orion (Bally et al. 2006). Bally et al. list several values for  $\dot{M}$  for each jet in their Table 6 that are derived with different assumptions; the values that we have plotted in Figure 32 correspond to  $\dot{M}_0$  in their Table 6 (multiplied by a factor of 2 to account for both sides of a bipolar jet, to be consistent with our estimates in Table 4). These values were derived using the same method adopted here (i.e., eqn. 2), and therefore provide a useful comparison, subject to the same uncertainties and potential systematic effects. The sample discussed by Bally et al. (2006) was studied with a similar *HST*/ACS survey in the F658N filter. It is also worth noting that this sample of Orion jets represents those found in the *outer* parts of the Orion Nebula, not in the brightest inner region near the Trapezium. The contrast between jets and the background nebula is therefore comparable to Carina.

The main lesson from Figure 32 is that in Carina we are likely missing a large number of HH jets at the lower end of the  $\dot{M}$  distribution, even with *HST*, if this distribution is similar to that in Orion. Both show a similar slope in the jet mass-loss function, with very roughly  $N \propto \dot{M}^{-0.5}$ . The  $\dot{M}$  distribution for Carina HH jets peaks at  $\sim 10^{-7.6} M_\odot \text{ yr}^{-1}$ , whereas that in Orion seems to peak at lower values around  $10^{-8.4} M_\odot \text{ yr}^{-1}$ . Orion is 5 times closer to us than Carina, so with the same *HST* camera, it is easier to detect fainter, thinner shock filaments and narrower jets that have lower mass-loss rates. The thin filaments of these weaker HH jets may be lost in the bright nebular background with the lower physical spatial resolution achieved in Carina. If the  $\dot{M}$  distribution in Orion is representative of the intrinsic distribution in Carina, then it is likely that the HH jets we have detected in Carina are roughly half (or less) of the total number of protostellar outflows in the region we surveyed. Our ACS H $\alpha$  survey did not uniformly cover the entire Carina Nebula, however, and is not an unbiased sample with any strict completeness criteria (see Figure 1). Nevertheless, it seems likely that we are missing a large number of weaker jets. Extrapolating from the 39 jets we detected with *HST*, correcting for both a factor of  $\sim 2$  because of undetected jets at the low end of the  $\dot{M}$  range plus the fact that we only surveyed a portion of the nebula with *HST*, it is likely that Carina currently harbors at least 150–200 active protostellar jets.

## 6 DISCUSSION

### 6.1 Jets from Tiny Cometary Globules

A key qualitative result of this study is that the *HST* images of Carina reveal several cases where HH jets emerge from tiny cometary clouds (roughly 0.01–0.05 pc in size). The most striking example was HH 900, but several other examples are seen as well, like HH 901, 1006, 1011, 1013, HHc-1, and HHc-3. The presence of a collimated HH jet emerging from such a globule requires that the globule harbor an actively accreting protostar, so it proves that even

the smallest clouds – which appear to be only shredded remnants of a larger molecular cloud — are, in fact, important sites of ongoing active star formation in an evolving H II region like Carina. Since the phase during which an active HH outflow may be detected is quite short (a few  $10^4$  yr) compared to the expected evaporation time of the cloud ( $>10^5$  yr), and because we are biased toward detecting the most powerful outflows (see above), it is possible that more of these small clouds also harbor young stars.

Interestingly, the clouds from which the jets emerge are small enough and isolated enough that they may be formation sites of a *single* star or binary system. This makes them valuable objects for case studies in star formation because their isolated nature simplifies the complexities normally encountered in crowded massive star-forming regions.

There is another reason that these objects may be of particular interest, having to do with the looming deaths of several nearby massive stars and possible connections to our own Solar System. As discussed above for the case of HH 900, these globules are destined to intercept the SN ejecta that will soon result from the deaths of  $\eta$  Car and several other massive stars that are only a few parsecs away. This can lead to efficient injection of radioactive nuclides into the tiny clouds, as is thought to have occurred in our own Solar System, making these objects possible analogs of the conditions that formed the Sun. In the specific case of HH 900, we showed in §3.2.2 that the cross-sectional size of its cloud would intercept a fraction of the SN ejecta from a hypothetical  $\eta$  Carinae SN that would be commensurate with the amount of SN ejecta thought to be injected into the cloud from which the Solar System formed. That estimate was for only a single SN, but Carina harbors  $\sim 70$  O stars (Smith 2006a), a few dozen of which are likely to explode in the next 1–2 Myr. These *multiple* SNe can greatly enhance the amount of young SN ejecta that will be imparted to these clouds. Without a second generation of stars forming at the periphery of a giant H II region, as seen in Carina, it would be difficult to recreate the conditions necessary for the birth of the Solar System. The proto-solar cloud must have been fairly close to a SN and the cloud itself must have cast a fairly wide net in order to intercept enough fresh SN ejecta.

Orion has also been discussed as a possible analog of the conditions under which the Solar System formed, where young low-mass stars are seen in close proximity to an O-type star. However, remember that although one sees young protoplanetary disks very close to an O-type star that will *eventually* explode as a SN, that O star in Orion ( $\theta^1$ C Ori) is still very young and not ready to explode yet. By the time it evolves off the main sequence and ends its life 5–6 Myr from now, the Trapezium will likely have dissolved and the proplyds we see now will have long since had their disks evaporated. In Carina, on the other hand, several of the most massive stars are already 3 Myr old and appear poised to explode in short order —  $\eta$  Car, in particular, is thought to be near its end. Furthermore, the region will not witness just one SN from  $\eta$  Car, but rather, in the next 1–2 Myr there will be a rapid succession of a few dozen SNe, several of them from some of the most massive stars known. This key difference makes a massive evolving H II region like Carina seem like the most promising analog for the cradle of the Solar System.

## 6.2 Bending of HH Jets...or Not

Protostellar outflows are not always straight. HH jets with a gentle S-shape bend can result from precession of the axis of the driving source (e.g., Devine et al. 1997), whereas cases in which both opposing flows in a bipolar jet bend in the same direction require an external agent. These types of bent jets, reviewed recently by Bally et al. (2006), are interesting as they provide a potential diagnostic of bulk flows of plasma in the surrounding environment. In other words, they serve as “wind socks” in H II regions. They have been compared to the head-tail systems of jets from radio galaxies. Several types of externally bent jets (as opposed to precessing jets) have been discussed.

Some collimated jets show a clear bend *toward* the center of star formation activity with increasing separation from the jet source, such as HH 499 and other jets in NGC 1333 (Bally & Reipurth 2001). In these cases the jet bend results because the young star that drives it is moving through a stationary ambient medium, as might occur if young star is dynamically ejected from the active star-forming cluster (Bally & Reipurth 2001).

In regions where young massive stars are present near a jet, such as in the Orion Nebula, jets tend to bend *away* from the massive O-type stars. In these cases, the bending may be caused by the influence of winds or UV radiation from the massive stars. This can occur by several mechanisms (see Bally et al. 2006), including the direct ram pressure of a side wind (stellar winds or a bulk flow of plasma in the H II region cavity), radiation pressure acting on dust grains entrained by the jet, or the rocket effect if neutral gas in the jet becomes ionized by UV radiation. All of these forces act to push the jet flow away from the massive stars that provide winds and radiation. Manifestations of this type of jet bending include the class of LL Ori objects (Bally et al. 2001), as well as smoothly curved bipolar jets like HH 502 (Bally et al. 2006) and HH 555 (Bally & Reipurth 2003).

A protostellar jet expanding away from its driving source may also bend suddenly if the jet has a grazing collision with a nearby cloud or other obstacle (another jet, another star’s disk, etc.). In this collision, the jet may be deflected in a different direction (e.g., Raga & Cantó 1996; Gouveia Dal Pino 1999). Examples of this phenomenon include the HH 110/270 combination (Rodriguez et al. 1998; Reipurth & Olberg 1991) and the HH 83/84 complex (Reipurth et al. 1997a).

Among the 39 known HH jets and jet candidates in Carina, we detect an interesting variety of jet bends. We discuss these in the context of three different types of jet bending, illustrated schematically in Figure 33, numbered according to the three cases discussed below:

1. First, our *HST* images reveal several examples of jets that bend *away* from nearby O-type stars, as expected in a region with rather harsh environmental conditions driven by the  $\sim 70$  O-type stars in Carina (Smith 2006a). This is the same as the case discussed above, exemplified by jets and LL Ori objects in Orion (Bally et al. 2006). See Bally et al. (2006) for quantitative estimates of the forces that bend such jets. Examples of this phenomenon in Carina include HH 901, 903, 1004, 1012, 1017, HHc-3, HHc-5, and HHc-8. Two of these, HH 1012 and HHc-8, appear to be true LL Ori objects. This class of bent jets tends to be found closer to

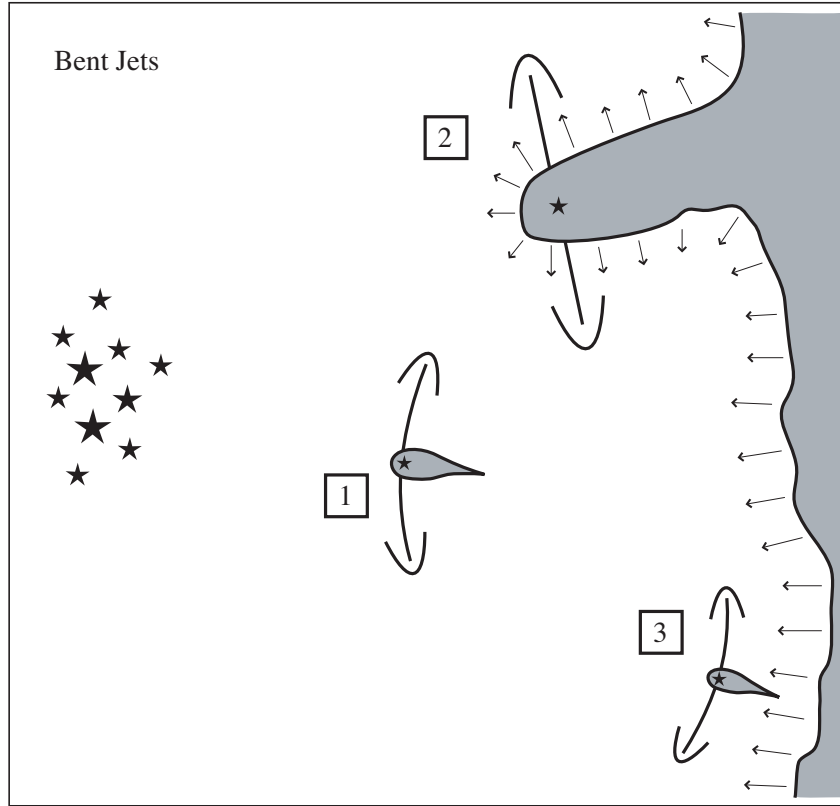


**Figure 33.** A schematic illustration referring to how HH jet axes may get bent by external mechanisms, as discussed in §6.2. A cluster of massive stars is located at left. Case 1 refers to a jet that is bent away from the massive stars by radiation or winds. Case 2 refers to a jet whose axis is not bent because it is moving through a diverging photoevaporative flow from the surface of a dust pillar, which may protect the jet from winds or inhibit its bending. Case 3 shows a jet axis that is bent toward the massive stars because it is located amid a strong photoevaporative flow from the surface of an adjacent molecular cloud, which effectively acts as a tail wind and dominates over the direct radiation or wind from the massive stars.

O stars, being more directly impacted by stellar winds and radiation.

2. Counter to expectations, several jets exhibit *no perceptible bend of their jet axis*, or very weak bends. These jets are surprisingly straight, considering the harsh environment in which they reside. A good example discussed previously is HH 666 (Smith et al. 2004c), which maintains a very straight jet axis as each of its bipolar flows moves more than a parsec from the point where the jet was launched. Other clear examples of straight bipolar jets among the new sample of jets and jet candidates in Carina are HH 902 and 1010. HH 902 does show some material that appears to be swept back in between clumps, but dense knots in the jet maintain a straight trajectory. These jets emerge from the heads of large dust pillars that have clearly been shaped by feedback from massive stars, so the straight axis is somewhat surprising. One possible explanation for the lack of any perceptible bend in the jets has to do with the immediate environment into which they are expanding once they exit the obscured part of the natal dust pillar. Namely, the bright-rimmed dust pillars are clearly irradiated by a strong UV flux, and probably have dense photoevaporative flows from their surfaces (depicted by short arrows in Figure 33). These dense photoevaporative flows from the head of a curved dust pillar will be radially divergent, so they will flow in essentially the same direction as any HH jet emerg-

ing from the pillar (i.e. normal to the surface of the pillar). Several dust pillars, such as the one associated with HH 666, show clear empirical evidence for dense flows in the form of streaks and striations proceeding radially from the irregular surface of the cloud. These flows will therefore exert no side force on the jet to divert its trajectory, and these dense photoevaporative flows may even *shield* the HH jet from the sideward ram pressure of a bulk flow of plasma in the larger wind-blown bubble. Around some pillar heads, one can see evidence for a stand-off shock between the photoevaporative flow and winds. Intermediate cases are also possible, as in HH 903, where the bulk flow of H II region plasma is in the process of crossing the pillar.

3. Lastly, we also see jets that – counter-intuitively – bend *toward* nearby massive stars. The best example of this, discussed earlier, is HH 900. This behavior is somewhat perplexing, because it is probably not attributable to dynamical ejection from that cluster as in the case of bent jets in NGC 1333 (Bally & Reipurth 2001). (In the case of HH 900, the cloud and its star would need to have been ejected from Tr 16, but the cluster is much older than the young cometary cloud, and the tail of HH 900 points away from Tr 16.) The explanation for this type of jet bend may be similar to the previous case — i.e. the influence of strong photoevaporative flows from the surfaces of molecular clouds. In this case, however, the dominant photoevaporative flow is not from



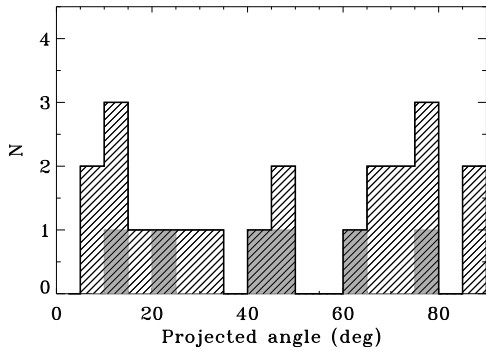


**Figure 34.** A histogram of the projected angle on the sky between the HH jet axis and the elongation of its parent cometary cloud or dust pillar. We have only plotted angles for 22 sources in which these angles could be determined (i.e. this does not include HH jets like those in NGC 3324, which emerge from a relatively straight ionization front). The hatched region includes all HH jets and candidates, while the shaded grey histogram shows the candidates alone.

the curved surface of the pillar or cloud from which the jet emerges, but from a neighboring cloud surface, as depicted for case 3 in Figure 33. HH 900 is located very close to the edge of a dark molecular cloud, which shows a very bright PDR at IR wavelengths, as we noted in §3.2.2. If HH 900 is embedded within this photoevaporative flow, the bulk flow could create the effective condition of a “tail wind” in its environment, so that the ram pressure pushes its bipolar jet toward the massive stars. While photoionizing radiation from O stars in Tr 16 has probably led to the initial sculpting of the cometary cloud and its tail that points away from the massive stars, this tail wind may also be the agent responsible for producing the unusual zig-zags in the thin tail of HH 900’s parent globule (Figure 4) by acting to compress it from the opposite direction.

### 6.3 Jet Orientations and Selection Effects

Most of the HH jets in Carina emerge from elongated cometary clouds or dust pillars, and some of the most striking examples are bipolar jets whose axis is nearly perpendicular to the elongated dust pillar. One may naturally wonder if there is any correlation between the jet axis orientation and the orientation of the underlying cloud (and hence, the direction toward the massive stars whose radiation has shaped it). In fact, as this paper was nearing completion, Lora, Raga, & Esquivel (2009) proposed that just such a preferential alignment should exist. This was based on 3D simulations of the interaction between an advancing ionization front and a neutral cloud, wherein compressed clumps of gas that form at the unstable interface tend to collapse and have angular momentum vectors perpendicular to the direction of the radiation flow. The clouds themselves tend to be elongated in the same direction as the radiation flow, forming structures akin to cometary clouds and dust pillars. If cores in these clumps collapse to form protostars and accretion disks, Lora et al. (2009) infer that the resulting HH jets will have a preferential orientation perpendicular to the long axis of their cometary cloud or dust pillar. We can test this hypothesis with the large number of jets discovered in

a single region like Carina, many of which emerge from dust pillars or cometary clouds that betray their dominant direction of incident radiation. If true, the angle between the jet axis and the long axis of a dust pillar or cometary cloud should favor orientations near  $90^\circ$ .

Figure 34 shows a histogram of this projected angle measured in *HST* images. This includes all HH jets and jet candidates for which an approximate cloud axis and jet axis could be measured (i.e. this does not include HH jets like those in NGC 3324, which emerge from a relatively straight ionization front, nor does it include HH objects like HH 1009 or HHc-4, 7, and 9 that lack clear collimated jets; obviously HH 1017 and 1018 are not included because they have no associated dust pillar). We conclude from Figure 34 that in this sample, we detect no obvious correlation between the projected angles. There does not appear to be a preferred physical orientation between the jets and their parent clouds, at least not that we can detect. Two caveats are that the hypothesis of Lora et al. (2009) requires that the formation of the protostars driving the jets was triggered by the advancing ionization front. We do not know what fraction of the jet sources in Carina formed on their own and which ones were triggered. Furthermore, the physical angle between the jet axis and its dust pillar is not necessarily the same as the angle projected on the sky. Even jets perpendicular to their dust pillars can be oriented in such a way that the angle between them projected on the sky is not  $90^\circ$ . One must either select jets known to have their dust pillar axis near the plane of the sky, or one must study the statistical distribution of angles for random projections.

In any case, we find no evidence that selection effects like the jet direction will bias the sample of jets detected in our images. One might imagine, for example, that jets emerging perpendicular to the axis of a cometary cloud would be easier to detect than those more closely aligned to its axis, but this is apparently not the case (e.g., HH 1006), so we consider it unlikely that we are missing a large number of jets whose axis is aligned with the cloud.

### 6.4 Energy, Momentum, and Turbulence Injection

Externally irradiated jets and outflows appear to be common in young H II regions. The Orion Nebula contains dozens of examples ranging from tiny, low mass-loss-rate jets visible only on high-angular resolution images such as those delivered by *HST* (Bally et al. 2006) to giant outflow lobes such as the parsec-scale HH 400 (Bally et al. 2001). The Carina Nebula also contains a growing collection of such jets and outflows (Smith, Bally, & Brooks 2004c; this work). However, the total momentum and energy injected by these outflows is unimportant in the global momentum and energy budget of the H II region. As in the Orion Nebula, momentum injection is dominated by the UV radiation field and stellar winds of the massive stars.

The mass injection rate of the Carina outflows ranges from less than  $\dot{M} \approx 2 \times 10^{-9} M_\odot \text{ yr}^{-1}$  to over  $2 \times 10^{-7} M_\odot \text{ yr}^{-1}$  per outflow. While the velocities for most outflows have not been determined by either spectroscopy or proper motions, typical values for such flows range from under  $100 \text{ km s}^{-1}$  to over  $400 \text{ km s}^{-1}$ . Radial velocity measurements for HH 666 indicate a range of velocities up to  $250 \text{ km s}^{-1}$  (Smith et al. 2004c). Using a relatively large value for pro-

tostellar outflows of  $\dot{M} = 2 \times 10^{-7} M_{\odot} \text{ yr}^{-1}$  and a flow velocity of  $200 \text{ km s}^{-1}$ , and assuming that at any typical time there are 100 active outflows in the region, the total rate of momentum injection into the nebula would be about  $\dot{P} = 4 \times 10^{-3} M_{\odot} \text{ km s}^{-2}$ . This is probably generous since this estimate used the outflow parameters near the maximum values observed, and assumes that only about 20% of the true number of flows have been detected.

The two dominant sources of internal motions in the nebula are likely to be the ionized photoevaporative/photoablation flows from dense cloud fragments trapped in the nebular interior and the impacts of massive-star winds. The average Lyman continuum luminosity of the Carina Nebula is about  $Q \approx 10^{51}$  ionizing photons per second (Smith 2006a; Smith & Brooks 2007); it may have been a bit higher while the three current WNH stars and  $\eta$  Car were main-sequence stars (see Smith 2006a). The total value of  $Q$  may have decreased by as much as 30% in recent times as three massive stars evolved into their WNH phase and  $\eta$  Car became an LBV with a cooler atmosphere/wind. The dusty Homunculus generated by the Great Eruption in the 1840s absorbs the UV luminosity of both this massive star and its companion, lowering the Lyman continuum luminosity by as much as 20% since the 1840s.

Photoablation-generated momentum injection into the Carina Nebula is determined by the incident flux of ionizing EUV ( $\lambda < 912 \text{ \AA}$ ) radiation. Dense spherical clouds lose mass to EUV photo-ablation at a rate

$$\begin{aligned} \dot{M}_p &\approx \zeta \pi r_p^2 \mu m_H n_e V_{II} \\ &= \zeta \mu m_H (3\pi Q/4\alpha_B)^{\frac{1}{2}} V_{II} r_p^{\frac{3}{2}} D^{-1}, \end{aligned} \quad (4)$$

where  $\zeta$  is a factor of order unity that accounts for the illumination geometry ( $\zeta \approx 1$  for a sphere illuminated from only 1 direction;  $\zeta=4$  for isotropic illumination from all directions),  $\mu \approx 1.35$  is the mean molecular weight,  $m_H$  is the mass of hydrogen,  $\alpha_B \approx 2.6 \times 10^{-13} \text{ cm}^3 \text{ s}^{-1}$  is the case-B recombination coefficient for hydrogen at  $10^4 \text{ K}$ ,  $D$  is the distance from the ionizing source with Lyman continuum luminosity  $Q$ , and  $V_{II} \approx 10$  to  $20 \text{ km s}^{-1}$  is the velocity of the photoablation flow. The electron density in the limit of a high-density spherical neutral condensation of radius  $r_p$  is given by

$$n_e = (3Q/4\pi\alpha_B)^{\frac{1}{2}} r_p^{-\frac{1}{2}} D^{-1}. \quad (5)$$

Assuming that there are about 100 dense globules and pillars photoablating in the nebular interior, that their typical radii are about  $r_p=0.2 \text{ pc}$ , and that they are located at an average distance of  $D=3 \text{ pc}$  from the nearest ionizing sources, dense gas injects plasma at a rate of order  $\dot{M} = 0.02 M_{\odot} \text{ yr}^{-1}$ . Assuming that these flows have a velocity given by the sound speed in the plasma implies a momentum injection rate  $\dot{P} \approx 0.25 M_{\odot} \text{ km s}^{-2}$ , two orders of magnitude larger than the injection rate by protostellar outflows.

Considering the growth of the  $M_{II} \approx 10^6 M_{\odot}$  H II region over the course of  $\tau \approx 3 \text{ Myr}$  by ionization of the surrounding molecular cloud complex implies  $\dot{M}_{II} \approx M_{II}/\tau \approx 0.3 M_{\odot} \text{ yr}^{-1}$  and  $\dot{P} \approx 1.2 M_{\odot} \text{ km s}^{-2}$ . This is at least three orders of magnitude larger than the injection rate by protostellar outflows. The force does not scale with  $\dot{M}$  due to the different geometry.

Finally, using a total stellar-wind mass injection rate of  $\dot{M}_{SW} = 1.4 \times 10^{-4} M_{\odot} \text{ yr}^{-1}$  (Smith & Brooks 2007; Smith 2006a) at a typical velocity  $V_{SW} = 10^3 \text{ km s}^{-1}$  for an O-type star, implies a momentum injection rate  $\dot{P}_{SW} \approx \dot{M}_{SW} V_{SW} \approx 0.14 M_{\odot} \text{ km s}^{-2}$ , comparable to the injection rate by photoablating clumps. The observed protostellar outflow sources inject momentum at a rate less than  $10^{-4}$  times the rate of combined injection rate from photoablation and massive star winds. They are therefore globally unimportant, even if our survey has left a large number of smaller jets undetected. Numerical studies suggest that HH jets can be significant in the global turbulence of a cloud (e.g., Wang et al. 2009), but our study indicates that this can only apply up to the time when massive stars are born, at which point HH jets become globally negligible. They may still be important locally, within clouds in outer parts of the nebula that are shielded behind ionization fronts.

While HH jets do not contribute significantly to the energy and momentum budget of the region, they do have a role to play. The presence of outflows in Carina provides important corroborating evidence for ongoing star formation in the dense clouds in and surrounding the nebula. They provide important diagnostics of physical conditions and nebular flows. They are the “wind socks” that serve to trace the motions of plasma, and the forces that act on various plasma components. The direction and amount of bending probes the forces acting on the jet beams and outflow lobes. Furthermore, the structure and properties of the jets and their source globules may provide diagnostics of the recent radiation history of the Carina Nebula. This topic will be addressed in a future paper.

## 7 CONCLUSIONS

Based on a narrow-band  $H\alpha$  imaging survey of the Carina Nebula with *HST*/ACS, we have reported the discovery of 38 new HH jets and candidate jets. Including the one jet that was previously discovered in ground-based data, HH 666 (Smith et al. 2004c), there are 22 HH jets and 17 candidate HH objects. We described each jet and its respective environment in detail. With assumed outflow speeds, we use the imaging data to derive the distribution of mass-loss rates for this sample of jets. A comparison with a similar distribution in Orion, where narrow shock filaments can be resolved more easily, shows that our survey is insensitive to jets with mass-loss rates below  $10^{-8} M_{\odot} \text{ yr}^{-1}$ . We must have missed several other jets, since this was a targeted study that did not cover the nebula uniformly. Conservatively, there may be 150–200 active protostellar jets in Carina.

This large number of jets signifies active outflow activity in Carina, and the short lifetime of these outflows suggests that there is a large population of accreting young protostars and YSOs in the region. We expect future IR studies to detect the driving sources of these HH jets, plus numerous other embedded YSOs from which HH jets are not seen. YSOs that are embedded within small dark clouds in the South Pillars offer a likely analog to the cradle of the Solar System, based on their proximity to a large number of very massive stars that will explode in the near future, polluting these clouds with radioactive nuclides like the  $^{60}\text{Fe}$  seen in Solar System chondrites. While we detected a few objects

that are true proplyds like the ones seen in Orion, especially in the core of Tr 14, there are a large number of small dark clouds that probably contain young stars. We also discussed the bending (or not) of HH jets exposed to feedback in giant H II regions and how the shaping of the jets depends on their location relative to bulk flows of plasma throughout the region. In particular, we find that photoevaporative flows from the surfaces of molecular clouds and dust pillars can significantly affect a jet's morphology for sources near the periphery of a giant H II region. Lastly, we evaluated the contribution of mass, energy, and turbulence injection by HH jets in Carina, finding that jets are negligible compared to winds and radiation from massive stars. The list of objects discovered provides the largest sample of irradiated outflows in a giant H II region, and followup studies with IR imaging and optical spectroscopy will characterize the physics of outflows exposed to feedback in a region like that where the Sun formed, and where most stars are born.

## ACKNOWLEDGMENTS

HH catalog numbers are assigned by B. Reipurth in order to correspond with the list of Herbig-Haro objects maintained at <http://ifa.hawaii.edu/reipurth/>, and we appreciate his patience in trying to assign consecutive HH numbers to our non-consecutive requests. We acknowledge input during early phases of this project from J.A. Morse, and we appreciate the help of the Hubble Heritage team at STScI in generating the color images in Figures 2 and 20. Support was provided by NASA through grants GO-10241 and GO-10475 from the Space Telescope Science Institute, which is operated by the Association of Universities for Research in Astronomy, Inc., under NASA contract NAS5-26555.

## REFERENCES

- Allen, D.A. 1979, *MNRAS*, 189, 1
- Bally, J., & Devine, D. 1994, *ApJ*, 428, L65
- Bally, J., & Reipurth, B. 2001, *ApJ*, 546, 299
- Bally, J., & Reipurth, B. 2003, *AJ*, 126, 893
- Bally, J., Heathcote, S., Reipurth, B., Morse, J.A., Hartigan, P., & Schwartz, R. 2002, *AJ*, 123, 2627
- Bally, J., Johnstone, D., Joncas, G., Reipurth, B., & Mallen-Ornelas, G. 2001, *AJ*, 122, 1508
- Bally, J., Licht, D., Smith, N., & Walawender, J. 2005, *AJ*, 129, 355
- Bally, J., Licht, D., Smith, N., & Walawender, J. 2006, *AJ*, 131, 473
- Brandner, W., Grebel, E.K., Chu, Y.H., Dottori, H., Drandl, B., Richling, S., Yorke, H.W., Points, S.D., & Zinnecker, H. 2000, *AJ*, 119, 292
- Boss, A.P., Ipatov, S.I., Keiser, S.A., Myhill, E.A., & Vanhala, H.A.T. 2008, *ApJ*, 656, 119
- Calvet, N. 1997, *IAUS*, 182, 417
- Calvet, N., Hartmann, L., & Strom, S.E. 2000, *Protostars and Planets IV*, p. 377
- Cameron, A.G.W., & Truran, J.W. 1977, *Icarus*, 30, 447
- Cantó, J., Rodríguez, L.F., Barral, J.F., & Carral, P. 1981, *ApJ*, 244, 102
- Currie, D.C., et al. 1996, *AJ*, 112, 1115
- Davidson, K., & Humphreys, R.M. 1997, *ARAA*, 35, 1
- de Gouveia Dal Pino, E.M. 1999, *ApJ*, 526, 862
- Desch, S.J., & Ouellete, N. 2005, *Lunar Plant. Sci. Conf.*, 36, 1327
- Devine, D., Bally, J., Reipurth, B., & Heathcote, S. 1997, *AJ*, 114, 2095
- Eisloffel, J., & Mundt, R. 1997, *AJ*, 114, 280
- Feinstein, A., Marraco, H.G., & Muzzio, J.C. 1973, *A&A*, 12, 331
- Foster, P.N., & Boss, A.P. 1996, *ApJ*, 468, 784
- Hamaguchi, K., Corcoran, M.F., Ezoe, Y., Townsley, L., Brooks, P., Gruendl, R., Vaidya, K., White, S.M., Strohmayr, T., Petre, R., & Chu, Y.H. 2009, *ApJ*, 695, L4
- Hartigan, P., Morse, J.A., & Raymond, J.C. 1994, *ApJ*, 436, 125
- Hartigan, P., Morse, J.A., & Bally, J. 2000, *AJ*, 120, 1436
- Hartigan, P., Morse, J.A., Reipurth, B., Heathcote, S., & Bally, J. 2001, *ApJ*, 559, L157
- Hartigan, P., Morse, J.A., Tumlinson, J., Raymond, J., & Heathcote, S. 1999, *ApJ*, 512, 901
- Hartmann, L., & Kenyon, S.J. 1985, *ApJ*, 299, 462
- Heathcote, S., Morse, J.A., Hartigan, P., Reipurth, B., Schwarz, R.D., Bally, J., & Stone, J.M. 1996, *AJ*, 112, 1141
- Hester, J.J., et al. 1996, *AJ*, 111, 2349
- Hester, J.J., Desch, S.J., Healy, K.R., & Leshin, L.A. 2004, *Science*, 304, 1116
- Klein, R.I., McKee, C.F., & Colella, P. 1994, *ApJ*, 420, 213
- Lee, T., Papanastassiou, D.A., & Wasserburg, G.J. 1976, *Geophys. Res. Lett.*, 3, 109
- Lopez, J.A., & Meaburn, J. 1986, *RevMexAA*, 13, 27
- Lora, V., Raga, A.C., & Esquivel, A. 2009, preprint (arXiv:0906.4368v1)
- Maíz Apellániz, J., Úbeda, L., Walborn, N.R., & Nelan, E.P. 2005, arXiv:astro-ph/0506283
- Marcolini, A., Strickland, D.K., D'Ercole, A., Heckman, T.M., & Hoopes, C.G. 2005, *MNRAS*, 362, 626
- Marti, J., Rodrigues, L.F., & Reipurth, B. 1993, *ApJ*, 416, 208
- Masciadri, E., & Raga, A. 2001, *AJ*, 121, 408
- Massey, P., & Johnson, J. 1993, *AJ*, 105, 980
- Megeath, S.T., Cox, P., Bronfman, L., & Roelfsema, P.R. 1996, *A&A*, 305, 296
- Morse, J.A., Hartigan, P., Cecil, G., Raymond, J.C., & Heathcote, S. 1994, *ApJ*, 399, 231
- Morse, J.A., Hartigan, P., Heathcote, S., Raymond, J.C., & Cecil, G. 1994, *ApJ*, 425, 738
- Morse, J.A., et al. 1998, *AJ*, 116, 2443
- Mundt, R., Ray, T.P., & Raga, A.C. 1991, *A&A*, 252, 740
- O'Dell, C.R. 2001, *ARA&A*, 39, 99
- Ogura, K. 1995, *ApJ*, 450, L23
- Pittard J.M., Falle, S.A.E.G., Hartquist, T.W., & Dyson, J.E. 2009, *MNRAS*, 394, 1351
- Poetzel, R., Mundt, R., & Ray, T.P. 1989, *A&A*, 224, L13
- Raga, A.C., & Cantó, J. 1996, *MNRAS*, 280, 567
- Rathborne, J.M., Brooks, K.J., Burton, M.G., Cohen, M., & Bontemps, S. 2004, *A&A*, 418, 563
- Reipurth B., & Olberg, M. 1991, *A&A*, 246, 535
- Reipurth B., & Bally, J. 2001, *ARA&A*, 39, 403
- Reipurth B., Bally, J., & Devine, D. 1997a, *AJ*, 114, 2708
- Reipurth B., Hartigan, P., Heathcote, S., Morse, J.A., & Bally, J. 1997b, *AJ*, 114, 757
- Reipurth B., Bally, J., Fesen, R.A., & Devine, D. 1998, *Nature*, 396, 343
- Reipurth, B., Heathcote, S., Morse, J.A., Hartigan, P., & Bally, J. 2002, *AJ*, 123, 362
- Rodríguez, L.F., Reipurth, B., Raga, A.C., & Cantó, J. 1998, *RevMexAA*, 34, 69
- Smith, N. 2002, *MNRAS*, 331, 7
- Smith, N. 2006a, *MNRAS*, 367, 763
- Smith, N. 2006b, *ApJ*, 644, 1151
- Smith, N., & Brooks, K.J. 2007, *MNRAS*, 379, 1279
- Smith, N., & Conti, P.S. 2008, *ApJ*, 679, 1467
- Smith, N., Egan, M.P., Carey, S., Price, S.P., Morse, J.A., & Price, P.A. 2000, *ApJ*, 532, L145
- Smith, N., Bally, J., & Morse, J.A. 2003, 587, L105
- Smith, N., Morse, J.A., & Bally, J. 2005a, *AJ*, 130, 1778
- Smith, N., Bally, J., Licht, D., & Walawender, J. 2005b, *AJ*, 129, 382
- Smith, N., Stassun, K.G., & Bally, J. 2005, *AJ*, 129, 888
- Smith, N., Bally, J., Shuping, R.Y., Morris, M., & Kassis, M. 2005d, *AJ*, 130, 763

- Smith, N., Barbá, R.H., & Walborn, N.R. 2004a, MNRAS, 351, 1457
- Smith, N., et al. 2004b, ApJ, 605, 405
- Smith, N., Bally, J., & Brooks, K.J. 2004c, AJ, 127, 2793
- Tachibana, S., & Huss, G.R. 2003, ApJ, 588, L41
- Vanhala, H.A.T., & Boss, A.P. 2000, ApJ, 538, 911
- Vanhala, H.A.T., & Boss, A.P. 2002, ApJ, 575, 1114
- Walawender, J., Bally, J., Reipurth, B., & Aspin, C. 2004, AJ, 127, 2809
- Walborn, N.R. 2009, in *Eta Car and the Supernova Impostors*, ed. K. Davidson & R.M. Humphreys (Springer), in press
- Walborn, N.R., et al. 2002, AJ, 123, 2754
- Walborn, N.R., Smith, N., Howarth, I.D., Kober, G.V., Gull, T.R., & Morse, J.A. 2007, PASP, 119, 156
- Walborn, N.R., & Liller, M.H. 1977, ApJ, 211, 181
- Wang, P., Li, Z., Abel, T., & Nakamura, F. 2009, prprint (arXiv:0908.4129)